CALPHAD: Computer Coupling of Phase Diagrams and Thermochemistry 89 (2025) 102836

Contents lists available at ScienceDirect

Calphad

journal homepage: www.elsevier.com/locate/calphad

Application of polyhedron model to predict heat capacity of mixed oxides☆

Jesus Alejandro Arias-Hernandez [a], Sun Yong Kwon [b], Elmira Moosavi-Khoonsari [a,*]

[a] Department of Mechanical Engineering, École de Technologie Supérieure (ÉTS), 1100 Notre-Dame St W, Montreal, Quebec, H3C 1K3, Canada
[b] Materials Science and Technology Division, Oak Ridge National Laboratory, TN, 37830, USA

ARTICLE INFO

Handling Editor: Prof. Z.K. Liu

Keywords:
Heat capacity
Oxides
Polyhedron Model
Thermodynamics
Second-order transitions

ABSTRACT

The heat capacity of mixed oxides can be estimated using a linear summation of the heat capacities of their structural constituent polyhedra. This approach is particularly useful for hygroscopic and volatile oxides, where experimental data can be difficult to obtain. The present work aims to enhance the polyhedron model (PM) by incorporating contributions from second-order transitions, including magnetic and site order-disorders, into C_p and expanding it to include ZnO and PbO-containing systems in comparison to the previous version of the model. A regression analysis was performed over the new dataset consisting of the properties of 85 compounds in the system Li-Na-K-Ca-Mg-Mn-Fe-Pb-Zn-Al-Ti-Si-O to obtain optimized C_p for 20 constituent polyhedra. We validate the updated PM against experimental data, demonstrating an overall improvement between 7 and 9 % in the estimation of C_p compared to the previous version of the model. We also compare the updated model with well-established models in the literature, such as the Neumann-Kopp Rule, and ab-initio calculations. The PM shows higher precision than NKR and the linear summation nature of PM endows the model with simplicity which contrasts with ab-initio calculations. Additionally, the model has demonstrated an inherent self-correction capability relative to the original input values, as shown for $K_2Si_4O_9$. The model is also applied to predict the heat capacity of 10 compounds in the Na_2O-PbO-SiO_2 and Na_2O-ZnO-SiO_2 systems, where experimental data are lacking.

1. Introduction

The heat capacity (C_p) of oxides is an essential thermodynamic property for understanding and optimizing a range of applications, such as solar thermal energy systems [1,2], cladding materials and ceramic fuels in nuclear reactors [3,4], semiconductors [5,6], photovoltaic cells [7,8], glassmaking [9,10], geophysics and planetary science [11,12], and pyrometallurgy [13,14]. Despite its importance, the C_p of many oxides remain undetermined due to experimental challenges such as hygroscopicity, volatility, and the lengthy synthesis processes [15,16]. To address these limitations, ab-initio calculations are widely used to estimate the thermodynamic properties including C_p. In particular, the Density Functional Theory (DFT) [17,18] and Molecular Dynamics (MD) [19] simulations are actively researched; however, both methods are computationally demanding and fall short in estimating thermodynamic properties at high temperatures as compared to experimental measurements [20].

To effectively prototype thermodynamic properties, empirical models based on experimental data have been developed. These models use a linear combination of constituent elements [21], oxides [21–23], iso-structural minerals [24], or elements differentiated by their coordination numbers (i.e., polyhedra) [25–30]. Neumann-Kopp Rule (NKR) is particularly prominent for approximating C_p values. NKR involves a weighted summation of the C_p values of the constituent oxides to calculate the C_p of binary or higher-order compounds [22]. Leitner et al. [31,32] compared NKR estimates with available experimental data for C_p of oxides, concluding that, near ambient temperatures, NKR provides an estimate with an average error of 3.3 %. However, the error can exceed 5 % at higher temperatures far from 298 K or for compounds where lattice vibrations and dilatation are not the only contributions to

☆ This manuscript has been authored by UT-Battelle, LLC under Contract No. DE-AC05-00OR22725 with the U.S. Department of Energy. The United States Government retains and the publisher, by accepting the article for publication, acknowledges that the United States Government retains a non-exclusive, paid-up, irrevocable, world-wide license to publish or reproduce the published form of this manuscript, or allow others to do so, for United States Government purposes. The Department of Energy will provide public access to these results of federally sponsored research in accordance with the DOE Public Access Plan (http://energy.gov/downloads/doe-public-access-plan).

* Corresponding author.
E-mail address: Elmira.moosavi@etsmtl.ca (E. Moosavi-Khoonsari).

https://doi.org/10.1016/j.calphad.2025.102836
Received 30 November 2024; Received in revised form 7 May 2025; Accepted 8 May 2025
Available online 20 May 2025

C_p such as in the case of $LaFeO_3$, $ErFeO_3$, and $HoFeO_3$. Furthermore, Helgeson et al. [24,33] proposed a method that yields errors within ±2 % for calculating C_p at 298 K by using a set of iso-structural minerals as constituents. Berman and Brown [23] estimated C_p for binary oxides as a function of temperature through a linear regression-based model, calculating the contribution of each unary oxide. However, Garofalo et al. [34] further analyzed Berman and Brown's model and reported significant deviations from experimental measurements with root mean squared errors (RMSE) between 29.82 $J\,mol^{-1}K^{-1}$ and 44.63 $J\,mol^{-1}K^{-1}$.

Robinson et al. [35] proposed the polyhedron model (PM), which assumes that minerals can be presented as discrete constituent polyhedra with specific coordination numbers, maintaining invariant intrinsic properties across different structures. Hazen [36] further developed this model, addressing the effects of temperature and pressure on polyhedron properties, such as cation coordination numbers and distortions. Holland [26] highlighted the significance of non-lattice vibrational contributions, including magnetic and site second order-disorder transitions, which should be excluded in regression analyses aimed at determining the thermodynamic properties of constituent polyhedra. Moreover, Holland et al. [26] identified a correlation between entropy and molar volume, suggesting that structural factors might play a crucial role in thermodynamic properties. Later, Hinsberg et al. [27,28] applied the polyhedron model to assess the thermodynamic and physical properties of oxides and hydroxides, including ΔH^0_{298K}, S^0_{298K}, molar volume (V), and C_p. However, they did not account for non-vibrational contributions in their C_p calculations. Wu et al. [29] subsequently extended the polyhedron model to predict ΔH^0_{298K} and S^0_{298K} for titanates. Despite these advancements, the polyhedron model has not been further developed to encompass the C_p of oxides since Hinsberg's work [27]. Moreover, current polyhedron models primarily rely on a linear summation approach, ignoring additional contributions such as non-phononic (second order transitions) effects and interactions among constituent polyhedra in C_p calculations.

The present work aims to enhance the polyhedron model by incorporating second-order transitions into the C_p calculations, commonly observed in compounds such as gehlenite and leucite. A detailed analysis of the residuals is performed to identify the impediments of the polyhedron model in calculating C_p of compounds such as Na_4SiO_4, $K_2Si_4O_9$, $KAlSi_2O_6$, Li_2SiO_3, and $Li_2Ti_3O_7$. In addition, fifteen more titanates were included, i.e., in total twenty (compared to five in Hinsberg's model [27]), along with six PbO-containing oxides and three ZnO-containing oxides. This expansion considers Ti octahedra (Ti-Oct) and multiple sites for Pb and Zn cation polyhedra (Pb-multi and Zn-multi). The accuracy and predictability of the model are compared with the C_p values measured by experiments and those estimated using NKR and DFT. The strengths and limitations of the model are discussed. Furthermore, the model was applied to subsequently estimate the C_p of ten alkali lead silicate and alkali zinc silicate compounds, where no experimental data are available.

2. Methodology

2.1. Polyhedron model

The polyhedron model is based on the assumption that the thermodynamic properties including lattice vibrational C_p of ionic compounds can be calculated from the linear summation of the C_p of their constituent polyhedra [36,37]. Fig. 1 shows the structure of $PbSiO_3$ and $PbTiO_3$ compounds including their constituent polyhedra, i.e., Pb-multi (which refers to the possibility of finding Pb with multiple coordination numbers), Si-tetrahedra, or Ti-octahedra, where the C_p of the compounds were calculated by adding the values of their constituent polyhedra.

Therefore, the lattice vibrational C_p of mixed oxides, C_p^{LV}, can be calculated using Equation (1):

$$C^{LV}_{p,i}(T) = \sum n_j c_{p,j}(T), \tag{1}$$

where i represents the compound phase, and j the constituent polyhedron, $C^{LV}_{p,i}(T)$ is the heat capacity of the ionic compound as a function of temperature, n_j is the stoichiometry of the constituent polyhedron, and $c_{p,j}(T)$ is the heat-capacity of the constituent polyhedron j at a determined temperature. For example, the compound $PbSiO_3$ consists of PbO (Pb-multi) and SiO_2 (Si-tet) polyhedra, where $n_{Pb-multi} = 1$ and $n_{Si-tet} = 1$.

2.2. Second-order transitions and Landau theory

Second-order transitions, such as magnetic and site order-disorder transitions, are prevalent in many compounds and contribute to the C_p. These transitions are characterized by sharp peaks in the C_p curve, indicating a significant increase in the energy required to raise the temperature near the critical temperature. Given that the influence of second-order transitions on C_p is considerable, Landau theory should be used to describe their effects.

The magnetic order-disorder transition is commonly observed in oxides containing transition metals, such as Fe^{2+}, Fe^{3+} and Mn^{2+}. Previously, Holland et al. [26] and Powell et al. [40] took into account the magnetic contributions to the enthalpy and entropy of compounds [26,40]. This type of transition can occur at temperatures below room

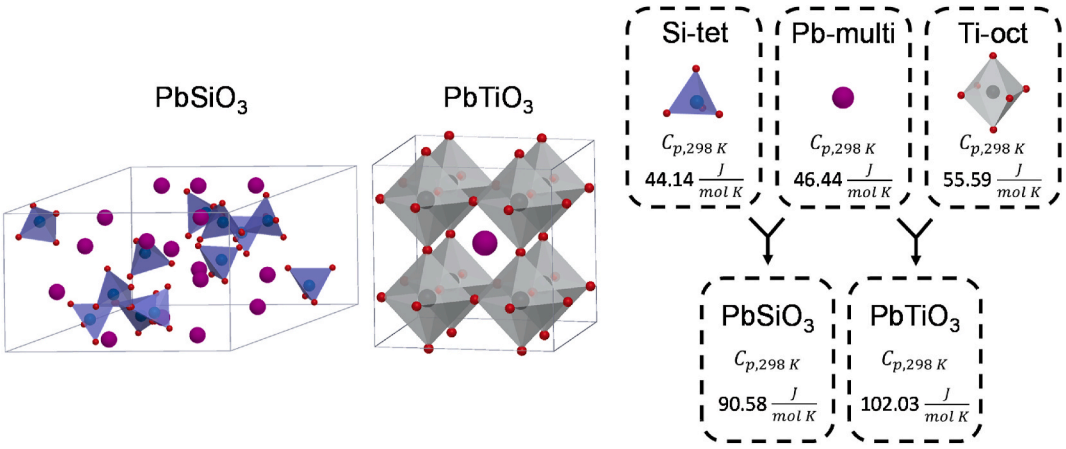

Fig. 1. Schematic presentation of constituent polyhedra of $PbSiO_3$ and $PbTiO_3$ compounds, Ti-octahedra, Si-tetrahedra, and Pb-multi, and the associated C_p values (constructed from Boucher et al. [38] and Wang et al. [39], respectively).

temperature, as seen in many Fe-bearing oxides such as $Ca_3Fe_2Si_3O_{12}$ [41], $CaFeSi_2O_6$ [42] and $Fe_2Si_2O_6$ [43], or above room temperature, as in the cases of magnetite (Fe_3O_4) [44], hematite (Fe_2O_3) [45], and NiZn-ferrites [46].

Another prevalent second-order transition is the site order-disorder transition, which is related to changes in the distribution of cations within the same crystal sub-lattice structure. This transition is characterized by a peak in the C_p curve at high temperatures [47]. Both magnetic and site order-disorder transitions above 298 K contribute to the high-temperature C_p of a compound.

The heat capacity of a compound that accounts for both the lattice vibrational C_p and the second-order contributions can be represented as

$$C_p = C_p^{LV} + C_p^{mag} + C_p^{sit}, \tag{2}$$

where C_p^{LV} is the lattice vibrational contributions to heat capacity, calculated using Equation (1). The excess contributions from magnetic (C_p^{mag}) and site order-disorder transitions $\left(C_p^{sit}\right)$, at different temperatures can be calculated using Landau theory, following the explanation by Carpenter [47]:

$$C_p^{mag} = \frac{TS_{max}^{magnetic}}{2\sqrt{T_{c,mag}}\sqrt{T_{c,mag}-T}}; \quad T < T_{c,mag} \tag{3}$$

$$C_p^{sit} = \frac{TS_{max}^{site}}{2\sqrt{T_{c,sit}}\sqrt{T_{c,sit}-T}}; \quad T < T_{c,sit} \tag{4}$$

where S_{max} is the maximum disorder entropy, $T_{c,mag}$ and $T_{c,sit}$ are the critical temperatures for the magnetic or site order-disorder transitions, respectively, and T is the temperature under analysis. At temperatures above $T_{c,mag}$, C_p^{mag} is assumed to be equal to zero. Similarly in the case of site order-disorder, at temperatures above $T_{c,sit}$, $C_p^{sit} = 0$. Additionally, we took the expression detailed by Ulbrich [48] for the ideal maximum value of the magnetic entropy in Equation (3) and the site-configurational entropy in Equation (4):

$$S_{max}^{magnetic} = R\sum n\, ln(2s+1), \tag{5}$$

$$S_{max}^{site} = -mR\sum X_i\, ln\, X_i, \tag{6}$$

where X_i is the mole fraction of species i in a specific sublattice, m is the multiplicity which represents the number of possible sublattice sites per molecule in which cation disorder can occur, s is the spin quantum number (e.g., 2, 5/2 and 5/2 for Fe^{2+}, Fe^{3+}, and Mn^{2+}, respectively), n is the number of moles of transition metal cations (such as Fe^{2+}, Fe^{3+}, and Mn^{2+}) in the given oxides, and R is the gas constant (8.314 $J\,mol^{-1}K^{-1}$). For example, to calculate S_{max}^{site} of albite ($NaAlSi_3O_8$), with this sublattice structure $[Na]^{multi}$ $[Al_{0.25}, Si_{0.75}]_4^{tet}$ $[O]_8$, the mol fraction of Al is 0.25 and Si is 0.75, and the multiplicity of the tetrahedra site is 4.

2.3. Selection of input data (polyhedra and C_p curves)

The compounds selected in this work and their constituent polyhedra are listed in Table A.1. The dataset includes eighty-five compounds in the system Li_2O-Na_2O-K_2O-CaO-MgO-MnO-FeO-Fe_2O_3-PbO-ZnOAl_2O_3-TiO_2-SiO_2. Among these compounds, fifty-eight were taken from FactSage version 8.2 [49] databases; more specifically, fifty-five were extracted from FToxid; if not available, they were taken from FactPS database (i.e., sixteen compounds). FactSage data have been developed in the last three decades by the critical evaluation and optimization of all available and reliable experimental data for the binary, ternary, and multicomponent systems following the CALPHAD (CALculation of PHAse Diagrams) method. The remaining fourteen compounds used in the model were not available in FactSage; therefore, they were taken from the compilation made by Berman and Brown [23]. The C_p terms were calculated for each compound using Equation (7) as mentioned by Hinsberg [27]:

$$C_p = a + bT + cT^{-2} + dT^{-0.5} + eT^2 + fT^{-3} \tag{7}$$

2.4. Regression analysis

The C_p terms obtained using Equation (7) were used as input data into the regression. Multiple least-squares linear regression was used to calculate the c_p of the constituent polyhedra (listed in Table A1) for a temperature range of 298–1100 K at 50 K intervals. To avoid training the model based on the extrapolation of some of the C_p data found in Table B1, the maximum temperature was set at 1100 K. Two metrics were used to analyze the regression results, including the Standard Error (SE) and Normalized Root Mean Square Error ($RMSE_N$).

The SE of each polyhedron's c_p was calculated using Equation (8), as follows:

$$SE_{C_{p\,j}(T)} = \left(\frac{S_i}{S_j}\right)\sqrt{\frac{1-R_i^2}{\left(1-R_j^2\right)(N-I-1)}} \tag{8}$$

where s_i is the standard error of the regression using all polyhedra, s_j is the standard error of the regression using every polyhedron except "j", R_i is the goodness of fitting, N the number of compounds in the regression, and I the number of types of polyhedra considered in total. This procedure is conducted for each polyhedron at 50 K intervals for a temperature range of 298–1100 K.

It is important to note that the SEs of polyhedra do not fully describe the uncertainty of the predictions. However, they serve as indicators of the uncertainty associated with estimating the regression coefficients [50] and are useful for comparing with previous work by Hinsberg et al. [27]. The SEs of the regression coefficients reflect the model's ability to estimate the value of each polyhedron at a specific temperature. A lower SE indicates a higher capacity for the model to accurately fit the polyhedron value, while a higher SE signifies lower precision in estimating the coefficients.

The analysis of residuals was conducted by calculating the RMSE for each compound. This metric is particularly sensitive to outliers, allowing us to identify compounds where the model's predictive capability is weaker. It is important to note that the residuals are extensive properties influenced by the molecular size; larger molecules with more atoms tend to have higher C_P values, which can disproportionately affect the residual analysis. To address this, we employed $RMSE_N$, which normalizes the residuals by dividing them by the number of atoms, as described by Equation (9):

$$RMSE_{N,i} = \frac{\sqrt{\frac{\sum\left(C_{p\ (predict),i} - C_{p\ (exp),i}\right)^2}{n}}}{N_i}, \tag{9}$$

where n is the number of observations (and calculations) in the temperature range from 298 to 1100 K (here, n is equal to seventeen), and N is the number of atoms in a given compound. This normalization standardizes the residuals across compounds and allows a more equitable comparison between molecules with different atomic counts. By focusing on the analysis of residuals per atom, we can more accurately assess the model's performance and identify potential outliers for further investigation. The units of $RMSE_N$ are expressed as $J\,mol^{-1}K^{-1}$ per mole of atoms.

3. Results

Fig. 2 displays the scatter plot resulting from the comparison of the C_p input values of the eighty-five oxides mentioned in Tables A.1 and B.1 and their back-calculated values using the polyhedron model at different temperatures. The training of the model was performed by excluding the

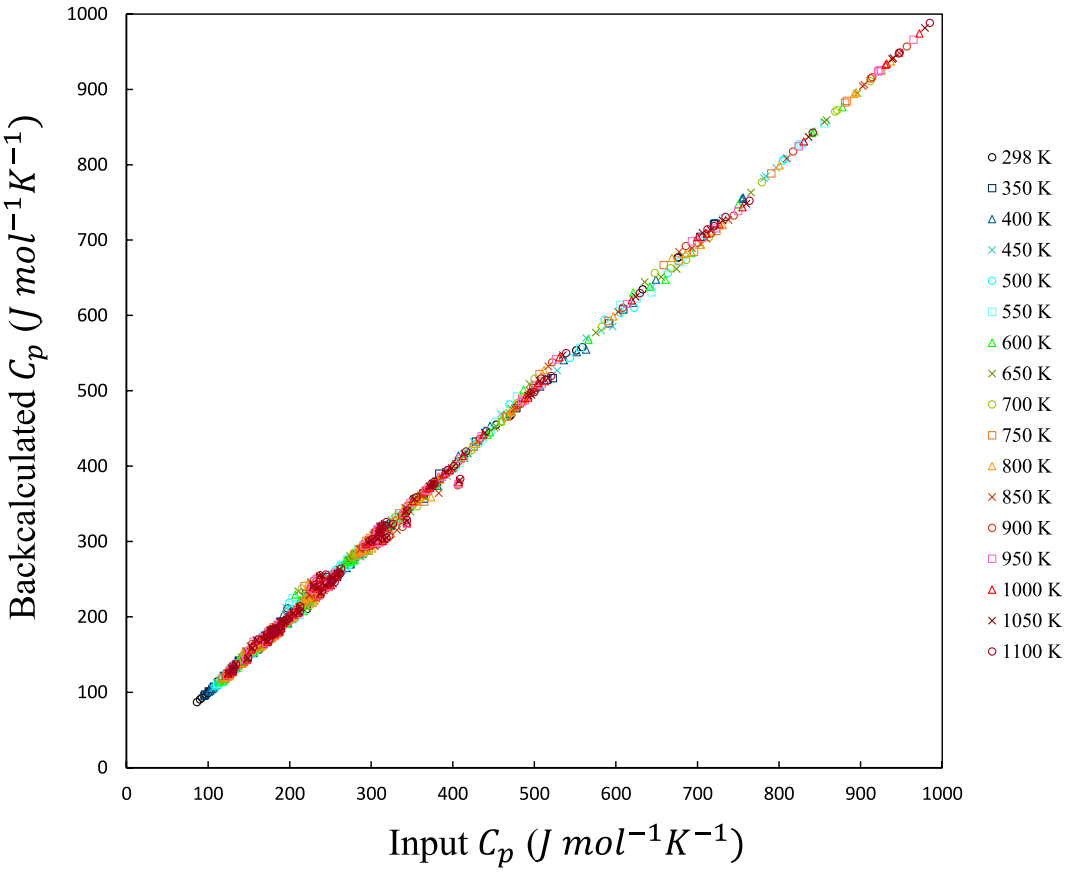

Fig. 2. Comparison between heat capacities of compounds (from FactSage 8.2 databases and Berman and Brown [23], given in Table B.1) and back-calculated values from the present polyhedron model at different temperatures.

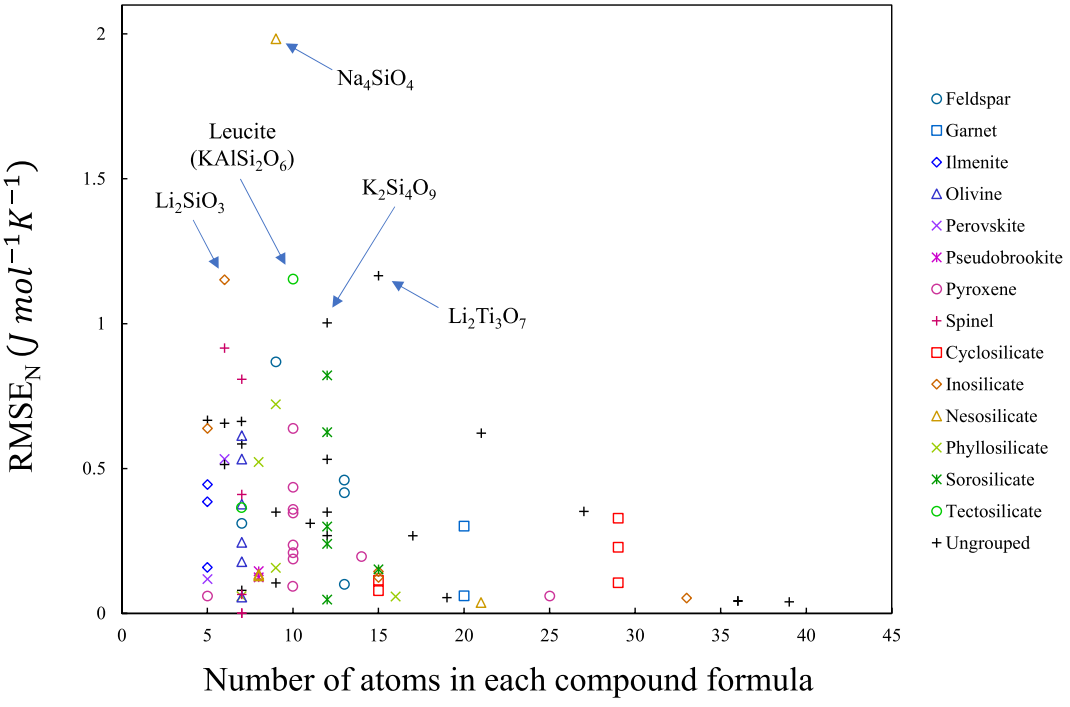

Fig. 3. Normalized root-mean-square errors ($RMSE_N$) between the C_p estimated by the present polyhedron model and the experimental data, listed in Tables A.1 and B.1. Each data point is the average error throughout the temperature range for each compound.

non-phononic contributions from the compounds such as leucite and gehlenite using Landau theory (Equations (2–6)(2-6)). The global errors across the analyzed temperature range are: Mean Square Error (MSE) of 26.39 ± 11.10 $\left(J\,mol^{-1}K^{-1}\right)^2$, RMSE of 5.0 ± 1.15 $J\,mol^{-1}K^{-1}$ and Mean Absolute Error (MAE) of 3.32 ± 0.67 $J\,mol^{-1}K^{-1}$. The highest errors occur at 950 K, while the lowest are observed at 350 K.

Fig. 3 displays the $RMSE_N$ between the predicted and ground truth C_p values of compounds, organized into various categories based on their crystal structures. A total of eighty-five compounds were classified into fourteen mineral groups: feldspar, garnet, ilmenite, olivine, perovskite, pseudobrookite, pyroxene, spinel, cyclosilicates, inosilicates, nesosilicates, phyllosilicates, sorosilicates, and tectosilicates. Twenty-two compounds could not be associated with any specific mineral group. It should be noted that the model has been applied only to mixed oxides, i.e., oxides containing at least two different types of polyhedra. There are no limitations regarding the number of atoms present; however, the minimum number of atoms for the mixed oxides used in this study happened to be five. The results indicate that compounds with fewer atoms generally exhibit higher residuals. This may be due to the increased significance of second nearest-neighbor and higher-order cation-cation interactions in smaller compounds, an effect not accounted for in the polyhedron model, which considers only the contributions of first nearest neighbors (i.e., cation-anion interactions). Notably, some ungrouped compounds, such as $K_2Si_4O_9$ and $Li_2Ti_3O_7$ demonstrate greater deviations compared to those with similar crystal structures. Helgeson et al. [24] noted that isostructural summation-based models tend to yield lower errors when using compounds from similar structural classes or a well-distributed mix of compounds from different classes; alkali silicates were found among the compounds with higher residuals. Among the compounds with higher residuals are several alkali silicates, including Na_4SiO_4, $KAlSi_2O_6$, Li_2SiO_3, and $K_2Si_4O_9$. These compounds exhibit significant deviations regardless of their classification into the nesosilicate, tectosilicate, or inosilicate groups, or their unclassified status. Further analysis of these deviations is discussed in Section 4.2.

Table 1 presents the C_p values for each polyhedron as a function of temperature, along with the associated SE and R^2 values (goodness-of-fit) from the linear regression model at various temperatures. The R^2 values range from 0.9995 to 0.9999, indicating the highest residuals at 950 K and the lowest (i.e., the best fit) at 350 K. This suggests that C_p can be effectively modeled by summing the constituent polyhedra of a compound within the temperature range of 298–1100 K. The RMSE values show an increasing trend with rising temperature, ranging from 2.91 $J\,mol^{-1}K^{-1}$ at 350 K to 6.57 $J\,mol^{-1}K^{-1}$ at 950 K. Since PM considers only vibrational contributions and second order phase transitions contributions to C_p, this trend may be related to phenomena overlooked by PM, such as thermal expansion, anharmonic and electronic effects, which become more significant as temperature rises [51–53]. The data shows that Pb-multi (0.58 ± 0.14), Si-tet (0.60 ± 0.14), Na-multi (0.60 ± 0.14) and Ti-Oct (0.72 ± 0.17) have the lowest SE values, indicating higher precision in estimating the C_p s of these polyhedra. The first and second numbers in the parentheses indicate the average SE value over the temperature range specified above and its standard deviation. In contrast, Fe-tet (5.95 ± 1.38), Mn-tet (5.83 ± 1.35), Mg-tet (4.16 ± 0.96), Li-oct (2.60 ± 0.60), and Li-multi (4.35 ± 1.01) exhibit greater SE values, reflecting higher uncertainty in their estimations. It is also noteworthy that polyhedra associated with a larger number of compounds used to train the model can significantly influence the precision of heat capacity estimations.

Table 2 provides the temperature dependent C_p function for each optimized polyhedron fitted using Equation (7). To predict lattice vibrational C_p of a compound at a given temperature, the C_p of constituent polyhedra must be calculated using the data given in Table 2 according to Equation (7) at the target temperature and further summed, as explained in Equation (1).

Table 1(a)
Heat capacity values in $J\,mol^{-1}K^{-1}$ for polyhedra and their standard errors (temperatures are in K and RMSE are in $J\,mol^{-1}K^{-1}$).

Polyhedra	298	SE	350	SE	400	SE	450	SE	500	SE	550	SE	600	SE	650	SE	700	SE
Ti-oct	55.68	0.44	60.02	0.42	62.96	0.48	65.2	0.56	66.94	0.62	68.36	0.66	69.58	0.7	70.65	0.72	71.6	0.74
Si-tet	43.95	0.36	48.84	0.35	52.64	0.4	55.71	0.46	58.19	0.51	60.24	0.55	61.96	0.58	63.43	0.6	64.69	0.61
Al-tet	40.29	0.51	44.34	0.49	47.73	0.57	50.53	0.65	52.83	0.72	54.71	0.78	56.25	0.82	57.53	0.84	58.6	0.86
Al-oct	39.44	0.44	44.23	0.42	47.78	0.48	50.56	0.56	52.77	0.62	54.57	0.67	56.05	0.7	57.29	0.73	58.34	0.74
Fe3-oct	50.79	0.62	55.37	0.59	58.56	0.68	60.96	0.79	62.84	0.87	64.34	0.94	65.56	0.99	66.55	1.02	67.38	1.04
Fe-tet	42.93	3.62	43.63	3.44	44.67	3.98	45.85	4.6	47.04	5.11	48.2	5.49	49.28	5.77	50.29	5.96	51.22	6.1
Fe-oct	43.67	1	47.57	0.95	50.27	1.1	52.31	1.27	53.94	1.41	55.25	1.51	56.32	1.59	57.21	1.64	57.95	1.68
Mn-tet	46.07	3.55	46.86	3.38	47.69	3.91	48.46	4.51	49.15	5.01	49.76	5.39	50.29	5.66	50.75	5.85	51.16	5.98
Mn-oct	42.8	0.69	46.51	0.65	48.49	0.76	49.71	0.87	50.54	0.97	51.15	1.04	51.62	1.09	52.01	1.13	52.36	1.16
Mg-tet	40.52	2.54	40.65	2.41	41.27	2.79	42.08	3.22	43.02	3.58	43.97	3.85	44.89	4.04	45.76	4.17	46.56	4.27
Mg-oct	37.01	0.68	40.95	0.65	43.2	0.75	44.76	0.86	45.96	0.96	46.95	1.03	47.8	1.08	48.55	1.12	49.23	1.14
Ca-oct	42.63	0.67	44.69	0.64	46.2	0.73	47.41	0.85	48.46	0.94	49.36	1.01	50.14	1.06	50.82	1.1	51.42	1.12
Ca-multi	41.11	0.53	44.25	0.5	46.32	0.58	47.83	0.67	48.96	0.74	49.83	0.8	50.53	0.84	51.09	0.87	51.56	0.89
Li-tet	28.57	1.03	31.39	0.97	33.52	1.13	35.36	1.3	37.04	1.45	38.6	1.55	40.07	1.63	41.46	1.69	42.8	1.73
Li-oct	29.24	1.59	30.86	1.51	32.03	1.74	33.03	2.01	33.96	2.24	34.83	2.4	35.63	2.52	36.39	2.61	37.09	2.67
Li-multi	31.25	2.65	34.87	2.52	36.28	2.92	37.2	3.37	38.16	3.74	39.21	4.02	40.32	4.22	41.48	4.36	42.64	4.47
Na-Multi	34.38	0.37	36.18	0.35	37.73	0.4	39.03	0.47	40.16	0.52	41.11	0.56	41.92	0.59	42.61	0.61	43.2	0.62
K-multi	36.32	1.01	37.6	0.96	38.77	1.11	39.79	1.28	40.71	1.42	41.55	1.53	42.35	1.6	43.16	1.66	44.01	1.69
Pb-Multi	46.55	0.36	48.1	0.34	49.3	0.39	50.3	0.45	51.19	0.5	52	0.54	52.75	0.57	53.45	0.59	54.11	0.6
Zn-multi	40.44	0.94	42.9	0.89	44.49	1.03	45.69	1.19	46.66	1.32	47.47	1.42	48.17	1.49	48.8	1.54	49.37	1.58
R^2	0.9999		0.9999		0.9999		0.9998		0.9998		0.9998		0.9998		0.9998		0.9998	
RMSE	3.15		2.91		3.34		3.85		4.29		4.61		4.85		5.01		5.13	

Table 1(b)
Heat capacity values in $J\,mol^{-1}K^{-1}$ for polyhedra and their standard errors (temperatures are in K and RMSE are in $J\,mol^{-1}K^{-1}$).

Polyhedra	750	SE	800	SE	850	SE	900	SE	950	SE	1000	SE	1050	SE	1100	SE
Ti-oct	72.43	0.75	73.18	0.77	73.89	0.81	74.68	0.94	75.19	0.94	75.52	0.92	75.87	0.89	76.19	0.87
Si-tet	65.76	0.62	66.7	0.64	67.53	0.67	68.54	0.78	69.07	0.79	69.55	0.77	70.05	0.74	70.5	0.73
Al-tet	59.63	0.88	60.51	0.9	61.25	0.95	61.72	1.1	62.35	1.11	62.93	1.08	63.39	1.05	63.78	1.02
Al-oct	59.22	0.75	59.99	0.77	60.66	0.81	61.27	0.94	61.79	0.95	62.26	0.93	62.7	0.9	63.1	0.88
Fe3-oct	68.06	1.06	68.63	1.09	69.1	1.15	69.5	1.33	69.83	1.34	70.1	1.3	70.35	1.26	70.56	1.24
Fe-tet	52.13	6.2	52.97	6.37	53.73	6.69	54.52	7.76	55.13	7.81	55.81	7.6	56.46	7.37	57.07	7.22
Fe-oct	58.58	1.71	59.12	1.75	59.59	1.84	59.77	2.14	60.29	2.15	60.77	2.1	61.17	2.03	61.53	1.99
Mn-tet	51.53	6.08	51.86	6.25	52.15	6.56	52.51	7.61	52.71	7.66	53	7.46	53.31	7.24	53.6	7.09
Mn-oct	52.71	1.18	53.04	1.21	53.38	1.27	53.47	1.47	53.97	1.48	54.48	1.44	54.93	1.4	55.4	1.37
Mg-tet	47.26	4.34	47.91	4.46	48.5	4.68	48.93	5.43	49.51	5.47	50.09	5.32	50.59	5.16	51.06	5.06
Mg-oct	49.82	1.16	50.37	1.2	50.9	1.26	51.29	1.46	51.83	1.47	52.35	1.43	52.82	1.38	53.28	1.36
Ca-oct	51.99	1.14	52.5	1.17	52.96	1.23	53.17	1.43	53.67	1.44	54.13	1.4	54.5	1.36	54.83	1.33
Ca-multi	52.08	0.9	52.53	0.93	52.92	0.97	53.1	1.13	53.49	1.14	53.87	1.11	54.2	1.07	54.48	1.05
Li-tet	44.14	1.75	45.44	1.8	46.71	1.89	47.75	2.2	48.9	2.21	49.26	2.15	49.57	2.09	49.86	2.04
Li-oct	37.8	2.71	38.45	2.79	39.07	2.93	39.48	3.4	40.12	3.42	40.78	3.33	41.35	3.23	41.89	3.16
Li-multi	43.77	4.54	44.83	4.66	45.81	4.9	46.06	5.68	47.15	5.72	48.06	5.57	48.66	5.4	49.08	5.29
Na-Multi	43.75	0.63	44.24	0.65	44.66	0.68	44.88	0.79	45.31	0.79	45.74	0.77	46.09	0.75	46.42	0.73
K-multi	44.96	1.72	45.98	1.77	47	1.86	50.11	2.15	50.04	2.17	50.22	2.11	50.33	2.05	50.47	2.01
Pb-Multi	54.78	0.61	55.42	0.63	56.05	0.66	56.51	0.76	57.21	0.77	57.9	0.75	58.42	0.72	58.93	0.71
Zn-multi	49.93	1.6	50.45	1.65	50.94	1.73	51.32	2.01	51.81	2.02	52.29	1.97	52.82	1.91	53.33	1.87
R^2	0.9998		0.9998		0.9998		0.9997		0.9997		0.9997		0.9997		0.9997	
RMSE	5.21		5.35		5.63		6.52		6.57		6.39		6.20		6.07	

Table 2
Coefficients for calculating C_p (in $J\,mol^{-1}K^{-1}$) of optimized polyhedra in the format of Equation (7):
$C_p = a + bT + cT^{-2} + dT^{-0.5} + eT^2 + fT^3$.

Polyhedra	*a*	*b*	*c*	*d*	*e*	*f*
Ti-oct	1.78E+02	−1.24E-01	−1.94E+05	−1.59E+03	1.09E-04	−3.71E-08
Si-tet	2.66E+02	−1.79E-01	1.42E+06	−3.36E+03	1.24E-04	−3.61E-08
Al-tet	2.63E+02	−1.64E-01	1.95E+06	−3.52E+03	9.70E-05	−2.41E-08
Al-oct	1.49E+02	−5.49E-02	2.33E+05	−1.69E+03	2.72E-05	−5.52E-09
Fe3-oct	8.11E+01	1.60E-02	−7.57E+05	−4.33E+02	−1.84E-05	5.89E-09
Fe-tet	6.92E+01	1.82E-02	9.85E+05	−7.19E+02	−1.50E-05	5.10E-09
Fe-oct	−1.28E+01	1.18E-01	−1.30E+06	7.61E+02	−1.00E-04	3.35E-08
Mn-tet	8.69E+01	−1.17E-02	6.60E+05	−7.72E+02	−1.73E-06	3.31E-09
Mn-oct	−1.01E+02	1.57E-01	−3.07E+06	2.42E+03	−1.09E-04	3.43E-08
Mg-tet	−6.19E+01	1.68E-01	4.35E+03	1.08E+03	−1.30E-04	3.99E-08
Mg-oct	−1.46E+02	2.07E-01	−3.28E+06	2.92E+03	−1.37E-04	3.85E-08
Ca-oct	−5.81E+00	8.58E-02	−7.39E+05	6.29E+02	−6.56E-05	2.05E-08
Ca-multi	8.88E+01	−3.31E-02	−5.11E+05	−5.85E+02	2.23E-05	−5.10E-09
Li-tet	2.75E+02	−3.08E-01	1.34E+06	−3.32E+03	2.90E-04	−1.04E-07
Li-oct	−8.88E+01	1.52E-01	−1.34E+06	1.66E+03	−1.05E-04	3.07E-08
Li-multi	−7.53E+02	8.17E-01	−9.62E+06	1.19E+04	−5.17E-04	1.33E-07
Na-Multi	5.86E+01	2.15E-02	3.13E+05	−5.50E+02	−2.96E-05	1.23E-08
K-multi	1.14E+03	−1.35E+00	9.15E+06	−1.54E+04	1.08E-03	−3.43E-07
Pb-Multi	8.03E+01	−2.37E-02	6.27E+04	−5.07E+02	2.40E-05	−6.82E-09
Zn-multi	−3.63E+01	1.03E-01	−1.44E+06	1.18E+03	−7.26E-05	2.26E-08

4. Discussion

4.1. Analysis of standard error

The input data used by Hinsberg et al. [27] consists of 94 compounds (57 oxides and 37 hydroxides) coming from the databases developed by Chaterjee et al. [54], Berman et al. [23] and Holland et al. [40] However, in the present work, the data were mainly collected from FactSage 8.2 optimized databases and if not available Berman et al. [23]. Additionally, the second-order transitions are also considered in the present work, ignored by Hinsberg et al. [27] Moreover, the model was expanded to include ZnO and PbO oxides. Therefore, it is expected for the present PM to behave differently than the previous iteration. Fig. 4 shows the difference between the SE values for all polyhedra obtained by Hinsberg et al. [27] minus those calculated in this work versus temperature. A positive value from the calculated difference suggests better fitting achieved by the present work and thus better predictions and vice versa.

As shown in Fig. 4, the SE values of nine out of nineteen polyhedra improved across the analyzed temperature range, with the most significant improvements occurring at the lower temperatures. This could be due to the extraction of excess heat capacity at temperatures below the critical temperature of leucite (938 K), suggesting that subtracting non-phononic contributions results in higher precision for the polyhedra C_p. It is also noteworthy that, at the higher end of the temperature range, all polyhedra—except for Li-multi and Zn-multi—showed improvements or remained close to the values reported by Hinsberg et al. [27] The effect of excess heat capacity is negligible at temperatures above the critical temperatures of the compounds, given in Tables A1 and B1. Therefore, the improved performance of the model at higher temperatures may be attributed to two factors: 1) the exclusion of hydroxides from the present work, which may influence the SE values, such as the case of Na-multi or K-multi, which were primarily trained based on hydroxides by Hinsberg et al. [27,28], and 2) the inclusion of additional oxides (fifteen more for Ti-oct and two more for Fe3-oct). The SE for all polyhedra was significantly improved at 298 K, especially for Mn-tet (from 7.24 to 3.55), Fe-tet (from 7.24 to 3.62), Na-multi (from 3.32 to 0.37), Ti-Oct (from 2.99 to 0.44), and K-multi (from 3.07 to 1.01). However, the SE values

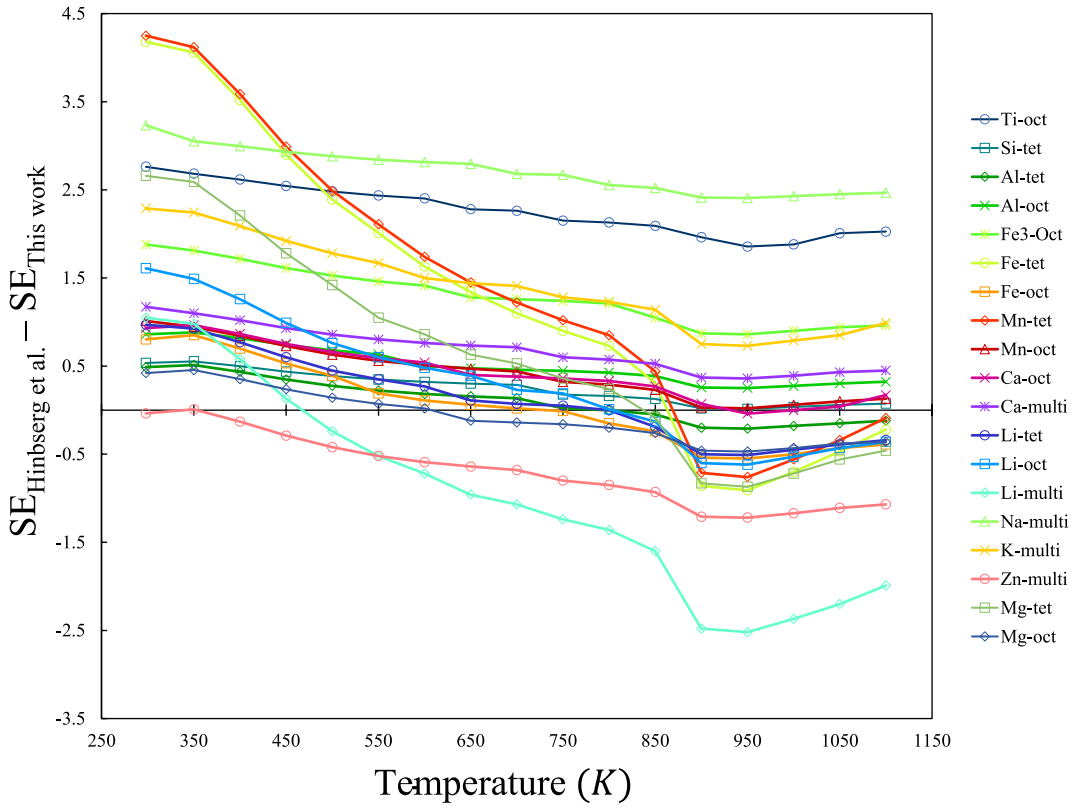

Fig. 4. Comparison of temperature-dependent SE values for evaluated polyhedra between Hinsberg et al. [27] and the present work.

for Al-tet, Li-oct, Li-tet, Fe-oct, Fe-tet, Mn-tet and Li-multi are higher than those reported by Hinsberg et al. [27] at temperatures above 700 K. These differences might be caused by the exclusion of hydroxides from the linear regression in the present work and having lower numbers of compounds containing the affected polyhedra for the regression analysis. All the polyhedra in our model, even those with a lower number of representative compounds, showed improvements compared to Hinsberg et al.'s model due to the inclusion of non-lattice vibrational contributions to C_p.

In the present work, Zn-multi has been considered, as Zn can exist in different sublattices [55–58] and the knowledge of the heat capacity of Zn-bearing compounds is limited to properly train different sublattices. The SE value for the Zn-multi polyhedron, averaged over temperature (1.5387 ± 0.3571), is higher than those for Zn-tet and Zn-oct reported by Hinsberg et al. [27] (0.85 ± 0.04 and 0.85 ± 0.04, respectively). However, Hinsberg et al. [27] did not report any Zn-containing compounds in their regression training list. Therefore, the correspondence of Zn-tet and Zn-oct to different compounds remains unclear.

4.2. Analysis of the outliers

The five compounds with the highest $RMSE_N$ values, (Li_2SiO_3, $K_2Si_4O_9$, $KAlSi_2O_6$, Na_4SiO_4, and $Li_2Ti_3O_7$), identified as outliers (see Fig. 3), are further analyzed. Fig. 5(a–e) compare the back-calculated C_p values from PM with the data from NKR, FactSage (FS), experimental data, and optimization results [59]. The NKR values were calculated by summing the C_p values of unary oxides obtained from FactSage FToxid (polymorphs used for the calculations are S1 for K_2O, quartz(l) for SiO_2, corundum for Al_2O_3, S1 for Na_2O, S1 for Li_2O, and rutile for TiO_2).

For $K_2Si_4O_9$, illustrated in Fig. 5(a), the back-calculated C_p values from PM are close to the NKR values and the experimental results from Fasshauer et al. [60] across the analyzed temperature range. Additionally, the back-calculated PM values have significantly improved compared to the original input data from FactSage FToxid (FS). Both PM and NKR demonstrate an average $RMSE_N$ of 1.41 and 1.21 $J\,mol^{-1}K^{-1}$, respectively, indicating approximately three times less error than the FS-FToxid curve when compared to the experimental data [60]. This suggests that the weight of the C_p values from K_2O and SiO_2 polyhedra in $K_2Si_4O_9$ taken from FactSage-FToxid has been normalized by other compounds with similar polyhedron constituents that have more accurate C_p values. At temperatures of 600 K and below, the PM is closer to the experimental values, while at high temperatures, NKR shows greater accuracy. As noted by Fasshauer et al. [60], $K_2Si_4O_9$ possesses a wadeite-type crystal structure where Si occupies both tetrahedral and octahedral sites at high pressures (5–6.5 GPa). The deviation of PM at elevated temperatures may arise from its assumption that silicon atoms are only surrounded by four oxygen cations. Furthermore, the optimization curve proposed by Kim et al. [62] shows a significant deviation from the other curves above 600 K, crossing over the FS values at 1000 K.

As seen in Fig. 5(b), for $KAlSi_2O_6$ (leucite), both PM and NKR show good prediction at temperatures below 650 K. NKR deviates from experimental data at temperatures between 700 and 950 K (around the critical temperature, 938 K), which is pertinent to the excess heat capacity. As explained before, a compound C_p is the summation of the lattice vibrational and second-order transition terms, thus PM, considering all these contributions, follows closely the experimental results, drastically increasing the C_p terms until the critical temperature. The deviations from the experimental values above the critical temperature may be related to a residual excess around the critical temperature (938 K) that Landau theory could not account for. This results in an overestimation of the C_p value above 938 K for K-multi by the PM during the model training.

For Li_2SiO_3 (see Fig. 5(c)), NKR shows a very good prediction in accordance with the experimental data for all the temperature ranges while PM deviates from the experiments at temperatures above 550 K. The calculated $RMSE_N$s between NKR, PM, and experimental measurements are 0.03 and 1.15 $J\,mol^{-1}K^{-1}$, respectively. The deviation shown

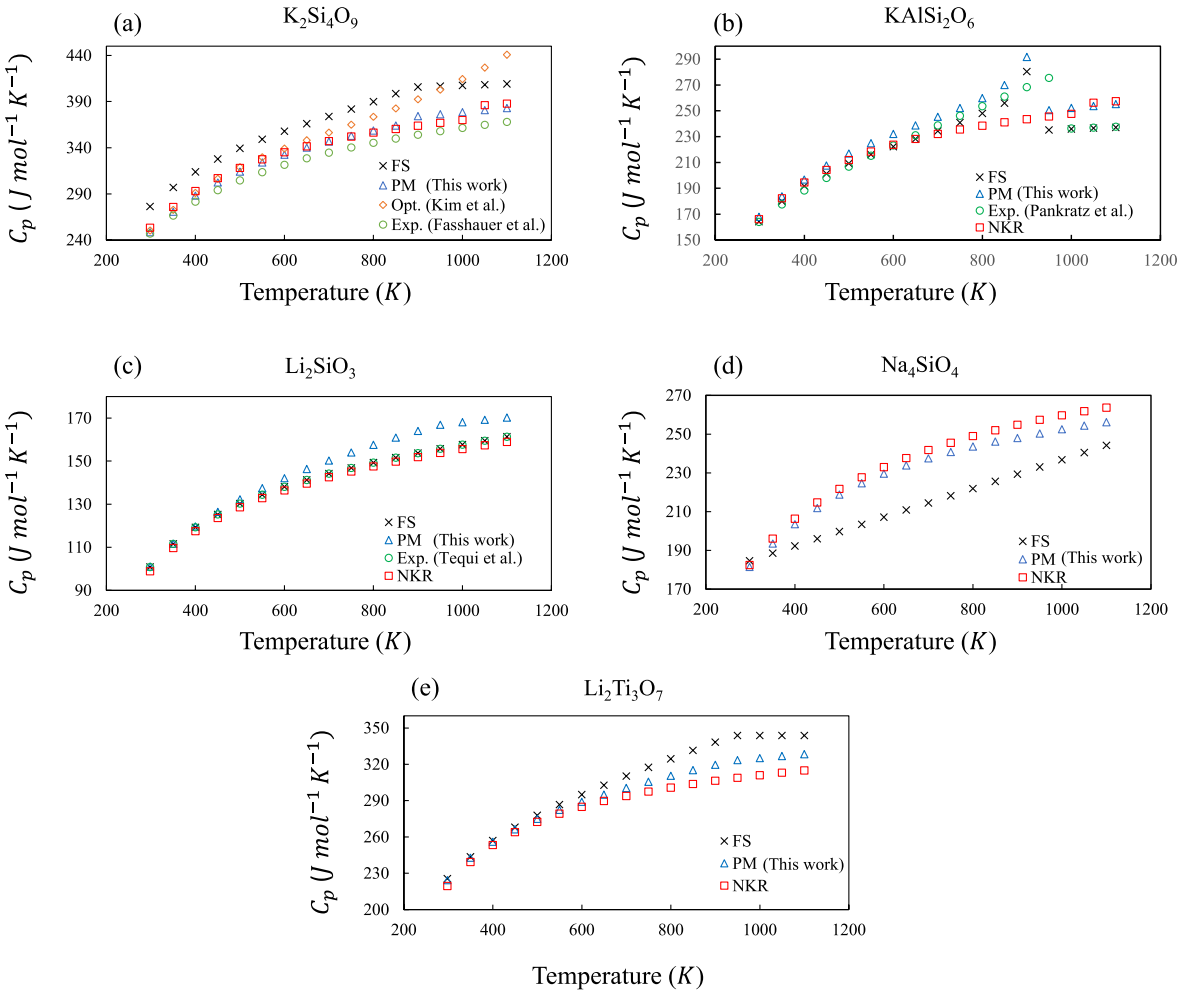

Fig. 5. Heat capacity versus temperature, back-calculated using PM, along with the data from NKR, FactSage (FS), experiments [60,61], and optimization [59]: (a) $K_2Si_4O_9$, (b) $KAlSi_2O_6$, (c) Li_2SiO_3, (d) Na_4SiO_4, and (e) $Li_2Ti_3O_7$. PM and NKR stand for polyhedron model and Neumann-Kopp Rule, respectively.

by PM could be caused by the distortion in Li-tet as mentioned by Tao et al. [63] who explained that the Li-O distances in such a polyhedron are distorted and could range between 1.937 Å and 2.755 Å at room temperature and possibly increase as temperature rises.

For Na_4SiO_4 (see Fig. 5(d)), no experimental measurements of C_p have been reported in the literature, and the average $RMSE_N$ between the input curve (FS) and the curves obtained from PM and NKR are 1.98 $J\ mol^{-1}K^{-1}$ and 2.50 $J\ mol^{-1}K^{-1}$, respectively. It is possible that similar to $K_2Si_4O_9$, the C_p values for Na_2O and SiO_2 polyhedra in Na_4SiO_4 taken from FactSage-FToxid have been normalized by other compounds with similar constituents that exhibit more accurate C_p values. Additionally, as reported by Kahlenberg [64], the Si-tet in Na_4SiO_4 are independent, and Na cations are coordinated by four or five oxygen atoms, classifying Na_4SiO_4 as a nesosilicate. However, when compared to other nesosilicates such as $PbZnSiO_4$, $CaTiSiO_5$ (sphene) or Al_2SiO_5 (sillimanite), which have $RMSE_N$ values of 0.05, 0.12, and 0.13 $J\ mol^{-1}K^{-1}$, respectively, the error for Na_4SiO_4 is notably higher. This could indicate that the C_p values from PM and NKR are more accurate than those from FactSage-FToxid.

Furthermore, for $Li_2Ti_3O_7$ (shown in Fig. 5(e)), PM, NKR, and input-FS show consistent C_p results at temperatures below 600 K. However, as the temperature increases, the deviation between the input curve and PM and NKR increases, which can be caused by the Ramsdellite-type crystal structure of $Li_2Ti_3O_7$. According to Tsuyumoto et al. [65], this compound is composed of distorted Ti-Oct chains with interstitial Li atoms, suggesting that distortion in polyhedra might lead to overestimation by the PM at high temperatures above 600 K, as also observed in Li_2SiO_3.

4.3. Validation of the polyhedron model

Predictions were made for four compounds, $Fe_3Al_2Si_3O_{12}$ (almandine), $KFeSi_2O_6$, Li_4SiO_4, and $NaAlSi_2O_6$, not included in the training set to analyze the predictive capacity of the PM, and the results are depicted in Fig. 6. NKR calculations were performed by using unary oxide values from FactSage (wüstite for FeO from FactPS, corundum for Al_2O_3, quartz (l) for SiO_2, S1 for K_2O and S1 for Li_2O from FToxid).

For the prediction of the $Fe_3Al_2Si_3O_{12}$ compound, Fe^{2+}-Oct, Si-tet, and Al-Oct were selected based on the crystal structure data from Zherebetskky et al. [66]. As shown in Fig. 6(a), the C_p values predicted by PM for $Fe_3Al_2Si_3O_{12}$ exhibit high accuracy across all temperatures, with an $RMSE_N$ of 0.22 $J\ mol^{-1}K^{-1}$ compared to the experimental values reported by Dachs et al. [67] The errors for the NKR calculations and the model from Hinsberg et al. [27] are 0.59 $J\ mol^{-1}K^{-1}$ and 0.25 $J\ mol^{-1}K^{-1}$, respectively. When compared to other compounds with garnet-like crystal structures, such as $Ca_3Fe_2Si_3O_{12}$ (andradite), which was used for model training and yielded $RMSE_N$ a value of 0.3 $J\ mol^{-1}K^{-1}$, the error for $Fe_3Al_2Si_3O_{12}$ is lower, highlighting the predictive strength of the PM.

Fig. 6(b) illustrates the C_p of $KFeSi_2O_6$ predicted by PM plus contributions from order-disorder transitions, alongside the C_p predicted by NKR and the experimental measurements. To compare the results

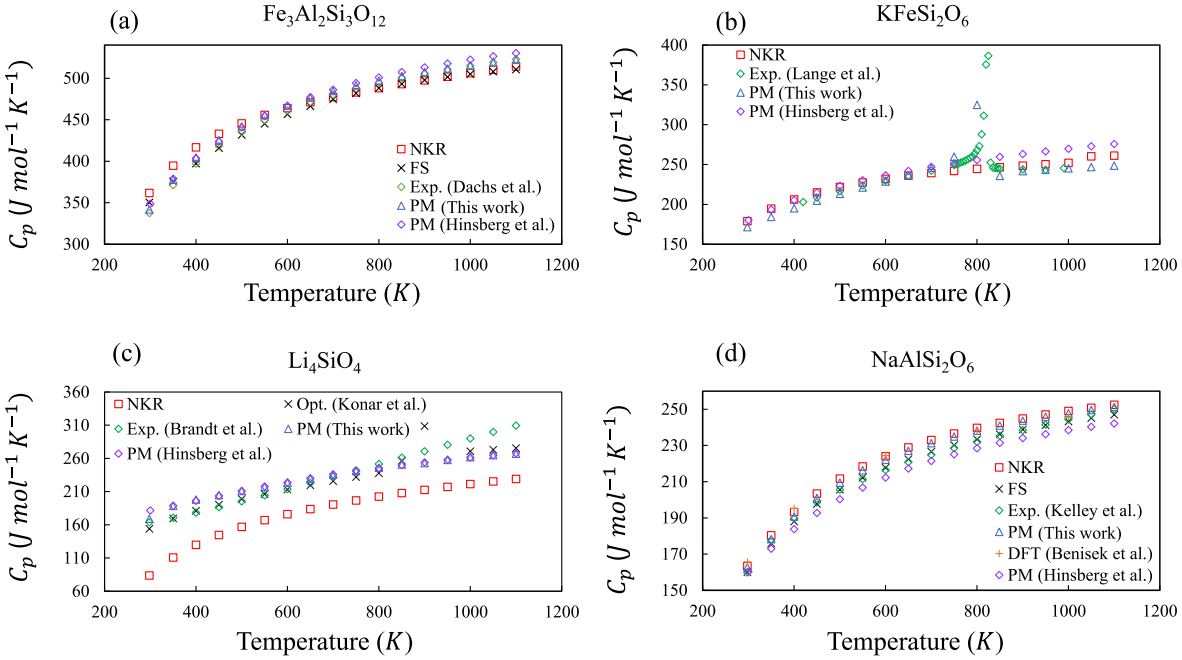

Fig. 6. Heat capacity versus temperature predicted by PM (this work), NKR, DFT [76], PM from Hinsberg et al. [27] thermodynamic optimization [77], and experimental values [67,68,72] for: (a) $Fe_3Al_2Si_3O_{12}$, (b) $KFeSi_2O_6$, (c) Li_4SiO_4 and (d) $NaAlSi_2O_6$.

obtained by Lange et al. [68] for $KFeSi_2O_6$ (an isostructural compound to leucite ($KAlSi_2O_6$)), an excess C_p value equal to that of leucite was added to the PM using Landau theory. Considering S_{max}, caused by Fe cation ordering in Si-tet sites (based on the explanation by Bell et al. [68] and Redfern et al. [69,70]), the PM provides slightly closer predictions than NKR through all the experimentally analyzed temperature range (400–1000 K), and considerable improvements in comparison to the work of Hinsberg et al. for temperatures above the critical temperature.

Fig. 6(c) presents the C_p of Li_4SiO_4 [71] predicted by PM, alongside the C_p calculated by NKR and the experimental measurements reported by Brandt et al. [72] The PM achieves an $RMSE_N$ of 2.16 $J\,mol^{-1}K^{-1}$ for C_p, showing deviation from experiments only at temperatures above 700 K. The NKR prediction for Li_4SiO_4 indicates a significant underestimation of the C_p, which yields an $RMSE_N$ of 2.79 $J\,mol^{-1}K^{-1}$. The model from Hinsberg et al. [27] compared to this study shows higher error of 2.19 $J\,mol^{-1}K^{-1}$ which can be attributed to the improvements of Si-tet in this work as observed in Fig. 4. Moreover, the C_p values predicted by PM align well with the curve proposed in the thermodynamic optimization of the Li_2O-SiO_2 system conducted by Konar et al. [73,74]

Fig. 6(d) depicts the C_p of $NaAlSi_2O_6$ predicted by PM, alongside values calculated by NKR, measured experimentally, and calculated using DFT at five different temperatures. All the models demonstrate good agreement with the experimental C_p values reported by Kelley et al. [75]. Notably, the PM shows better predictability than the DFT calculations from Benisek et al. [76] at temperatures below 600 K. However, DFT calculations exhibit higher precision at 1000 K. When compared to the NKR, PM consistently shows better predictability across all analyzed temperatures.

4.4. *Application of the polyhedron model to estimate the C_p of alkali lead- and zinc-silicate compounds*

The Na_2O-PbO-SiO_2 system has important applications in the recycling of lead-acid batteries [78], optics [79] and radiation shielding [80]. Within this system, six ternary compounds and their melting temperatures have been reported: $Pb_2Na_2Si_4O_{11}$ (903 K), $Pb_3Na_2Si_6O_{16}$ (990 K), $Pb_4Na_2Si_8O_{21}$ (813 K), $Pb_2Na_2Si_3O_9$ (888 K), $Pb_3Na_2SiO_6$ (962 K) and $Pb_2Na_2SiO_5$ (918 K) [81,82]. But their thermodynamic properties, including C_p, are not well established. The temperature in parentheses indicates the melting temperature of the compound. The PM developed in this work was utilized to calculate the C_p of these compounds until their melting point. The C_p data from PM in this work are shown in Fig. 7. Additionally, the heat capacity equations were derived, fitting to the C_p data.

In the other hand, the Na_2O-ZnO-SiO_2 system has gained interest in recent years due to its utilization in bioactive glasses [83] and its applications in biodiesel production [84]. In particular, zinc sodium silicate ($ZnNa_2SiO_4$) has demonstrated effectiveness as a cost-effective catalyst for this application, as noted by Rodriguez-Ramirez et al. [85]. Four ternary compounds, $ZnNa_2SiO_4$ (1613 K), $ZnNa_2Si_2O_6$ (1363 K), $ZnNa_4Si_2O_7$ (1133 K) and $Zn_2Na_4Si_3O_{10}$ (1248 K), have been reported for this system according to Holland et al. [86]. The temperature in parentheses indicates the melting temperature of the compound. The estimated C_p curves from the current PM are presented in Fig. 8. Predictions up to 1100 K were made using the current PM model, followed by extrapolation to higher temperatures up to the melting points of the compounds. Additionally, the heat capacity equations were derived, fitting to the C_p data.

5. Conclusions

The knowledge of thermodynamic properties such as heat capacity is important for advancing many areas of science and technology. Therefore, a model with interpolation and extrapolation capacity could be an alternative approach for calculating the heat capacity of unknown oxide compounds. In this work, we enhanced the polyhedron model by incorporating contributions from second-order transitions including magnetic and site order-disorders into heat capacity and expanding it to include ZnO and PbO-containing systems. The key highlights of this work are summarized below:

- Pb-multi and Zn-multi polyhedra and an additional fifteen titanates were included, compared to the work of Hinsberg et al. [27] The SE values improved across the entire temperature range for nine out of

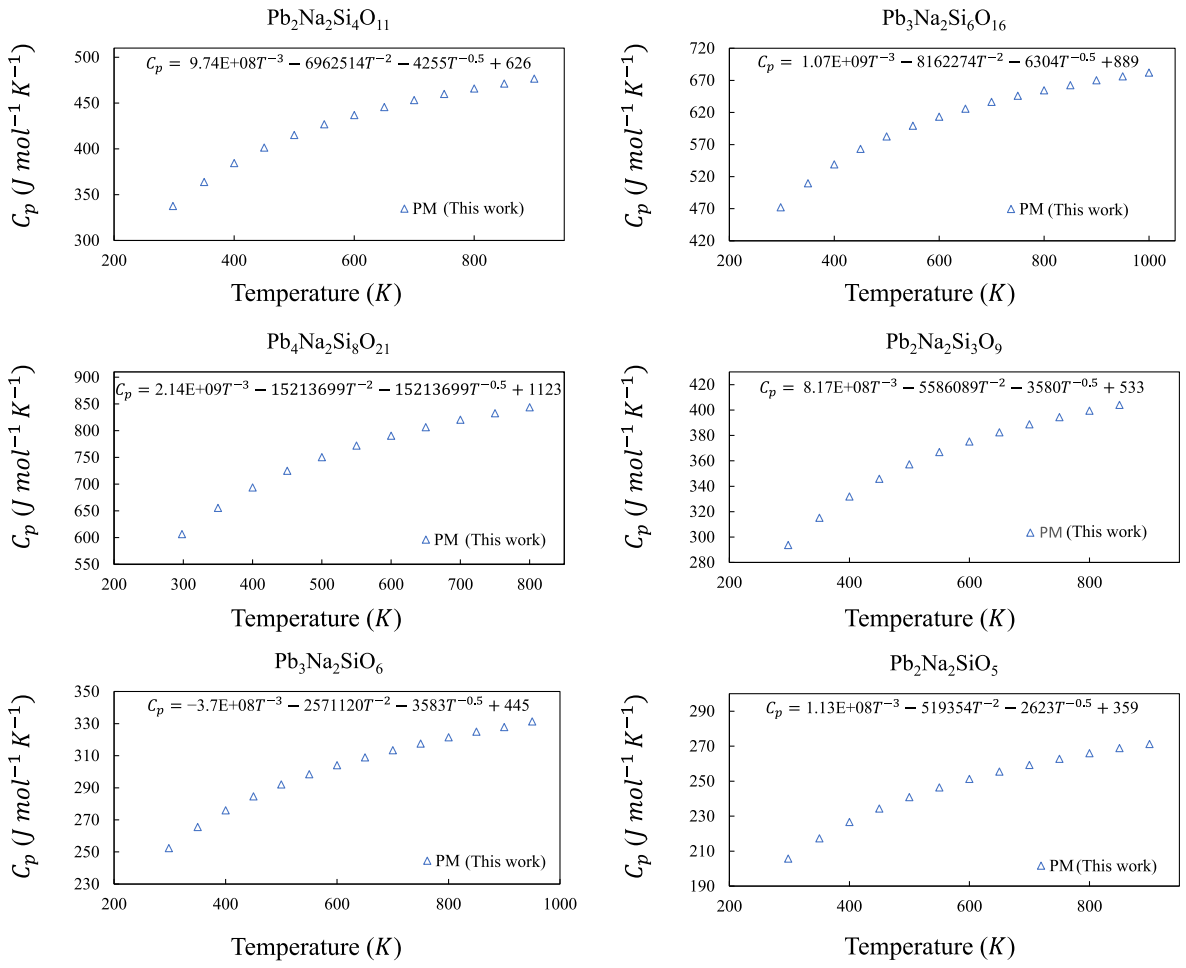

Fig. 7. Estimated heat capacity values versus temperature for the Na_2O-PbO-SiO_2 compounds using the PM developed in this work until their respective melting temperatures.

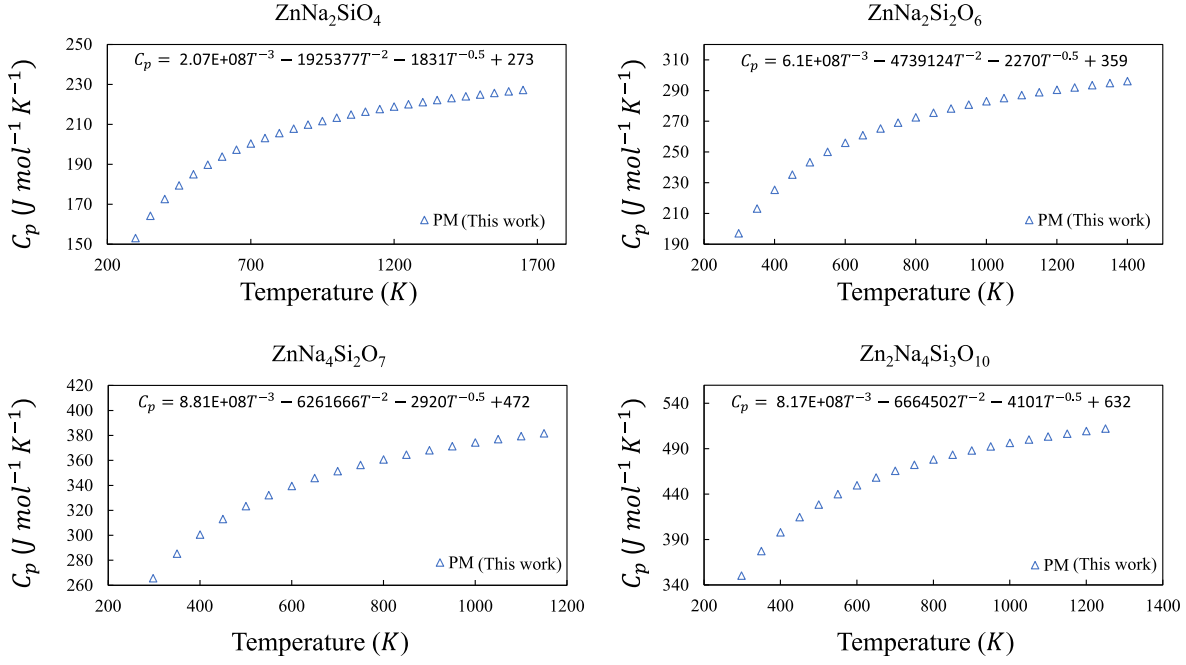

Fig. 8. Estimated heat capacity values versus temperature for the Na_2O-ZnO-SiO_2 compounds using the PM developed in this work.

nineteen polyhedra, while the remaining polyhedra exhibited similar values. This suggests a better fit of the input data, which significantly enhances the model predictability.

- A considerable improvement in C_p values was observed after Landau theory effectively accounted for the excess contributions from second-order transitions, including magnetic and site disorder. Compared to Hinsberg et al. [27], this improvement is particularly noticeable at temperatures between 298 and 850 K where the contribution of excess heat capacity is higher.
- The highest residuals were observed in the back-calculation of alkali-silicates, where the influence of biased data from FactSage FToxid affected the back-calculations of $K_2Si_4O_9$ and Na_4SiO_4.
- Furthermore, for $K_2Si_4O_9$, the modeled and back-calculated values from PM have shown significant improvement and a closer agreement with experimental data when compared to the original input data from FactSage. This demonstrates that the model has an inherent self-correction capability.
- The PM has demonstrated the ability to predict heat capacity over a wide temperature range. Its linear summation approach makes it relatively simple to implement, especially compared to DFT, which requires extensive calculations, and is typically limited to conditions near the ground state energy (0 K).
- While the PM demonstrates strong extrapolation capability, its limitations may lie in the lack of adaptability to structural transitions and the inability to account for second nearest neighbors and higher order interactions, atomic radii, bond distances, and polyhedron distortion effects. Incorporating these factors could further enhance the model's predictive accuracy. Moreover, since molar volume has shown a correlation with entropy [26], incorporation of molar volume into the model might improve the predictions of C_p.

CRediT authorship contribution statement

Jesus Alejandro Arias-Hernandez: Writing – review & editing, Writing – original draft, Visualization, Validation, Supervision, Software, Project administration, Methodology, Investigation, Formal analysis, Data curation, Conceptualization. **Sun Yong Kwon:** Writing – review & editing, Writing – original draft, Visualization, Validation, Supervision, Software, Project administration, Methodology, Investigation, Formal analysis, Data curation, Conceptualization. **Elmira Moosavi-Khoonsari:** Writing – review & editing, Writing – original draft, Visualization, Supervision, Resources, Project administration, Methodology, Investigation, Funding acquisition, Formal analysis, Conceptualization.

Declaration of competing interest

The authors declare the following financial interests/personal relationships which may be considered as potential competing interests: Elmira Moosavi-Khoonsari reports financial support was provided by Natural Sciences and Engineering Research Council of Canada. Sun Yong Kwon reports a relationship with UT-Battelle LLC that includes: employment. If there are other authors, they declare that they have no known competing financial interests or personal relationships that could have appeared to influence the work reported in this paper.

Acknowledgment

The authors would like to acknowledge the financial support of the NSERC Discovery Grant from the Government of Canada for this project. This manuscript has been authored by UT-Battelle, LLC under Contract No. DE-AC05-00OR22725 with the U.S. Department of Energy. The United States Government retains and the publisher, by accepting the article for publication, acknowledges that the United States Government retains a non-exclusive, paid-up, irrevocable, world-wide license to publish or reproduce the published form of this manuscript, or allow others to do so, for United States Government purposes. The Department of Energy will provide public access to these results of federally sponsored research in accordance with the DOE Public Access Plan (http://energy.gov/downloads/doe-public-access-plan).

Appendix A

Table A.1(a)
List of compounds and their constituent polyhedra used in this work.

Name	Compound	Ti-oct	Si-tet	Al-tet	Al-oct	Fe3-oct	Fe-tet	Fe-oct	Mn-tet	Mn-oct	Mg-tet	Mg-oct	Ca-oct	Ca-multi	Li-tet	Li-oct	Li-multi	Na-multi	K-multi	Pb-multi	Zn-multi
Sillimanite	Al_2SiO_5	0	1	1	1	0	0	0	0	0	0	0	0	0	0	0	0	0	0	0	0
Mullite	$Al_6Si_2O_{13}$	0	2	0	6	0	0	0	0	0	0	0	0	0	0	0	0	0	0	0	0
Gehlenite	$Ca_2Al_2SiO_7$	0	1	2	0	0	0	0	0	0	0	0	0	2	0	0	0	0	0	0	0
Akermannite	$Ca_2MgSi_2O_7$	0	2	0	0	0	0	0	0	0	1	0	0	2	0	0	0	0	0	0	0
Larnite	Ca_2SiO_4	0	1	0	0	0	0	0	0	0	0	0	2	0	0	0	0	0	0	0	0
	$Ca_2ZnSi_2O_7$	0	2	0	0	0	0	0	0	0	0	0	2	0	0	0	0	0	0	0	1
Andradite	$Ca_3Fe_2Si_3O_{12}$	0	3	0	0	2	0	0	0	0	0	0	0	3	0	0	0	0	0	0	0
Merwinite	$Ca_3MgSi_2O_8$	0	2	0	0	0	0	0	0	0	0	1	3	0	0	0	0	0	0	0	0
Rankinite	$Ca_3Si_2O_7$	0	2	0	0	0	0	0	0	0	0	0	0	3	0	0	0	0	0	0	0
Wollastonite	$Ca_3Si_3O_9$	0	3	0	0	0	0	0	0	0	0	0	3	0	0	0	0	0	0	0	0
	$Ca_3Ti_2O_7$	2	0	0	0	0	0	0	0	0	0	0	0	3	0	0	0	0	0	0	0
	$Ca_4Ti_3O_{10}$	3	0	0	0	0	0	0	0	0	0	0	0	4	0	0	0	0	0	0	0
Anorthite	$CaAl_2Si_2O_8$	0	2	2	0	0	0	0	0	0	0	0	1	0	0	0	0	0	0	0	0
Ca-tschermaks	$CaAl_2SiO_6$	0	1	1	1	0	0	0	0	0	0	0	1	0	0	0	0	0	0	0	0
Ca-walstromite (ps-wolastonite)	$CaCa_2(Si_3O_9)$	0	3	0	0	0	0	0	0	0	0	0	2	1	0	0	0	0	0	0	0
Hedenbergite	$CaFeSi_2O_6$	0	2	0	0	0	0	1	0	0	0	0	1	0	0	0	0	0	0	0	0
Diopside	$CaMgSi_2O_6$	0	2	0	0	0	0	0	0	0	0	1	1	0	0	0	0	0	0	0	0
Monticellite	$CaMgSiO_4$	0	1	0	0	0	0	0	0	0	0	1	1	0	0	0	0	0	0	0	0
Perovskite	$CaTiO_3$	1	0	0	0	0	0	0	0	0	0	0	0	1	0	0	0	0	0	0	0
Sphene	$CaTiSiO_5$	1	1	0	0	0	0	0	0	0	0	0	0	1	0	0	0	0	0	0	0
Ferrocordierite	$Fe_2Al_4Si_5O_{18}$	0	5	4	0	0	0	2	0	0	0	0	0	0	0	0	0	0	0	0	0
Ferrosillite	$Fe_2Si_2O_6$	0	2	0	0	0	0	2	0	0	0	0	0	0	0	0	0	0	0	0	0

Table A.1(b)
List of compounds and their constituent polyhedra used in this work.

Name	Compound	Ti-oct	Si-tet	Al-tet	Al-oct	Fe3-oct	Fe-tet	Fe-oct	Mn-tet	Mn-oct	Mg-tet	Mg-oct	Ca-oct	Ca-multi	Li-tet	Li-oct	Li-multi	Na-multi	K-multi	Pb-multi	Zn-multi
Fayalite	Fe_2SiO_4	0	1	0	0	0	0	2	0	0	0	0	0	0	0	0	0	0	0	0	0
Ulvöspinel	Fe_2TiO_4	1	0	0	0	0	1	1	0	0	0	0	0	0	0	0	0	0	0	0	0
Ferropseudobrookite	$FeTi_2O_5$	2	0	0	0	0	0	1	0	0	0	0	0	0	0	0	0	0	0	0	0
Ilmenite	$FeTiO_3$	1	0	0	0	0	0	1	0	0	0	0	0	0	0	0	0	0	0	0	0
Potassium disilicate	$K_2Si_2O_5$	0	2	0	0	0	0	0	0	0	0	0	0	0	0	0	0	0	2	0	0
	$K_2Si_4O_9$	0	4	0	0	0	0	0	0	0	0	0	0	0	0	0	0	0	2	0	0
Potassium metasilicate	K_2SiO_3	0	1	0	0	0	0	0	0	0	0	0	0	0	0	0	0	0	2	0	0
Leucite	$KAlSi_2O_6$	0	2	1	0	0	0	0	0	0	0	0	0	0	0	0	0	0	1	0	0
Microcline	$KAlSi_3O_8$	0	3	1	0	0	0	0	0	0	0	0	0	0	0	0	0	0	1	0	0
Kalsilite	$KAlSiO_4$	0	1	1	0	0	0	0	0	0	0	0	0	0	0	0	0	0	1	0	0
Virgilite	$Li(AlSi_2O_6)$	0	2	1	0	0	0	0	0	0	0	0	0	0	0	0	1	0	0	0	0
Petalite	$Li(AlSi_4O_{10})$	0	4	1	0	0	0	0	0	0	0	0	0	0	0	0	1	0	0	0	0
Lithium disilicate	$Li_2Si_2O_5$	0	2	0	0	0	0	0	0	0	0	0	0	0	2	0	0	0	0	0	0
Lithium metasilicate	Li_2SiO_3	0	1	0	0	0	0	0	0	0	0	0	0	0	2	0	0	0	0	0	0
Ramsdellite	$Li_2Ti_3O_7$	3	0	0	0	0	0	0	0	0	0	0	0	0	2	0	0	0	0	0	0
	Li_2TiO_3	1	0	0	0	0	0	0	0	0	0	0	0	0	0	2	0	0	0	0	0
Spodumene	$LiAl(Si_2O_6)$	0	2	0	1	0	0	0	0	0	0	0	0	0	0	1	0	0	0	0	0
Eucryptite	$LiAl(SiO_4)$	0	1	0	1	0	0	0	0	0	0	0	0	0	1	0	0	0	0	0	0
Cordierite	$Mg_2Al_4Si_5O_{18}$	0	5	4	0	0	0	0	0	0	0	2	0	0	0	0	0	0	0	0	0
Enstatite (ortho-enstatite)	$Mg_2Si_2O_6$	0	2	0	0	0	0	0	0	0	0	2	0	0	0	0	0	0	0	0	0
Forsterite	Mg_2SiO_4	0	1	0	0	0	0	0	0	0	0	2	0	0	0	0	0	0	0	0	0
Qandilite	Mg_2TiO_4	1	0	0	0	0	0	0	0	0	1	1	0	0	0	0	0	0	0	0	0
Pyrope	$Mg_3Al_2Si_3O_{12}$	0	3	1	1	0	0	0	0	0	0	3	0	0	0	0	0	0	0	0	0
Sapphirine	$Mg_4Al_{10}Si_2O_{23}$	0	2	5	5	0	0	0	0	0	0	4	0	0	0	0	0	0	0	0	0
Karooite	$MgTi_2O_5$	2	0	0	0	0	0	0	0	0	0	1	0	0	0	0	0	0	0	0	0
Geikielite	$MgTiO_3$	1	0	0	0	0	0	0	0	0	0	1	0	0	0	0	0	0	0	0	0

Table A.1(c)
List of compounds and their constituent polyhedra used in this work.

Name	Compound	Ti-oct	Si-tet	Al-tet	Al-oct	Fe3-oct	Fe-tet	Fe-oct	Mn-tet	Mn-oct	Mg-tet	Mg-oct	Ca-oct	Ca-multi	Li-tet	Li-oct	Li-multi	Na-multi	K-multi	Pb-multi	Zn-multi
Mn-cordierite	$Mn_2Al_4Si_5O_{18}$	0	5	4	0	0	0	0	0	2	0	0	0	0	0	0	0	0	0	0	0
Tephroite	Mn_2SiO_4	0	1	0	0	0	0	0	0	2	0	0	0	0	0	0	0	0	0	0	0
Tetragonal	Mn_2TiO_4	1	0	0	0	0	0	0	1	1	0	0	0	0	0	0	0	0	0	0	0
Rhodonite	$Mn_5Si_5O_{15}$	0	5	0	0	0	0	0	0	5	0	0	0	0	0	0	0	0	0	0	0
Pyroxmangite	$MnSiO_3$	0	1	0	0	0	0	0	0	1	0	0	0	0	0	0	0	0	0	0	0
Mn-pseudobrookite	$MnTi_2O_5$	2	0	0	0	0	0	0	0	1	0	0	0	0	0	0	0	0	0	0	0
Pyrophanite	$MnTiO_3$	1	0	0	0	0	0	0	0	1	0	0	0	0	0	0	0	0	0	0	0
Sodium disilicate	$Na_2Si_2O_5$	0	2	0	0	0	0	0	0	0	0	0	0	0	0	0	0	2	0	0	0
	$Na_2Ti_3O_7$	3	0	0	0	0	0	0	0	0	0	0	0	0	0	0	0	2	0	0	0
	$Na_2Ti_6O_{13}$	6	0	0	0	0	0	0	0	0	0	0	0	0	0	0	0	2	0	0	0
	Na_2TiO_3	1	0	0	0	0	0	0	0	0	0	0	0	0	0	0	0	2	0	0	0
	Na_2ZnO_2	0	0	0	0	0	0	0	0	0	0	0	0	0	0	0	0	2	0	0	1
Sodium orthosilicate	Na_4SiO_4	0	1	0	0	0	0	0	0	0	0	0	0	0	0	0	0	4	0	0	0
Sodium silicate	$Na_6Si_2O_7$	0	2	0	0	0	0	0	0	0	0	0	0	0	0	0	0	6	0	0	0
Monophyllosilicate	$Na_6Si_8O_{19}$	0	8	0	0	0	0	0	0	0	0	0	0	0	0	0	0	6	0	0	0
	$Na_8Ti_5O_{14}$	5	0	0	0	0	0	0	0	0	0	0	0	0	0	0	0	8	0	0	0
Albite	$NaAlSi_3O_8$	0	3	1	0	0	0	0	0	0	0	0	0	0	0	0	0	1	0	0	0
Nepheline	$NaAlSiO_4$	0	1	1	0	0	0	0	0	0	0	0	0	0	0	0	0	1	0	0	0
Aegirine (Acmite)	$NaFeSi_2O_6$	0	2	0	0	1	0	0	0	0	0	0	0	0	0	0	0	1	0	0	0
	$Pb_2Al_2O_5$	0	0	0	2	0	0	0	0	0	0	0	0	0	0	0	0	0	0	2	0
	$Pb_2Fe_2O_5$	0	0	0	0	2	0	0	0	0	0	0	0	0	0	0	0	0	0	2	0
	$Pb_2Fe_2Si_2O_9$	0	2	0	0	2	0	0	0	0	0	0	0	0	0	0	0	0	0	2	0
	Pb_2SiO_4	0	1	0	0	0	0	0	0	0	0	0	0	0	0	0	0	0	0	2	0
	$Pb_2ZnSi_2O_7$	0	2	0	0	0	0	0	0	0	0	0	0	0	0	0	0	0	0	2	1
	$Pb_3Ca_2Si_3O_{11}$	0	3	0	0	0	0	0	0	0	0	0	0	2	0	0	0	0	0	3	0

Table A.1(d)
List of compounds and their constituent polyhedra used in this work.

Name	Compound	Ti-oct	Si-tet	Al-tet	Al-oct	Fe3-oct	Fe-tet	Fe-oct	Mn-tet	Mn-oct	Mg-tet	Mg-oct	Ca-oct	Ca-multi	Li-tet	Li-oct	Li-multi	Na-multi	K-multi	Pb-multi	Zn-multi
	Pb_4SiO_6	0	1	0	0	0	0	0	0	0	0	0	0	0	0	0	0	0	0	4	0
	$Pb_8CaSi_6O_{21}$	0	6	0	0	0	0	0	0	0	0	0	0	1	0	0	0	0	0	8	0
	$Pb_8ZnSi_6O_{21}$	0	6	0	0	0	0	0	0	0	0	0	0	0	0	0	0	0	0	8	1
	$PbAl_2O_4$	0	0	0	2	0	0	0	0	0	0	0	0	0	0	0	0	0	0	1	0
Margarosanite	$PbCa_2Si_3O_9$	0	3	0	0	0	0	0	0	0	0	0	0	2	0	0	0	0	0	1	0
	$PbFe_4O_7$	0	0	0	0	4	0	0	0	0	0	0	0	0	0	0	0	0	0	1	0
Alamosite	$PbSiO_3$	0	1	0	0	0	0	0	0	0	0	0	0	0	0	0	0	0	0	1	0
Larsenite	$PbZnSiO_4$	0	1	0	0	0	0	0	0	0	0	0	0	0	0	0	0	0	0	1	1
Willemite	Zn_2SiO_4	0	1	0	0	0	0	0	0	0	0	0	0	0	0	0	0	0	0	0	2
	Zn_2TiO_4	1	0	0	0	0	0	0	0	0	0	0	0	0	0	0	0	0	0	0	2
Gahnite	$ZnAl_2O_4$	0	0	0	2	0	0	0	0	0	0	0	0	0	0	0	0	0	0	0	1
Zinc ferrite	$ZnFe_2O_4$	0	0	0	0	2	0	0	0	0	0	0	0	0	0	0	0	0	0	0	1

Appendix B

Table B.1(a)
C_p terms of the compounds used for training the Polyhedron model. The coefficients shown have been rounded for presentation, but the exact values were used in the regression analysis.

Name	Compound	T^{-3}	T^{-2}	T^{-1}	$T^{-0.5}$	T^0	T^1	T^2	T^3	T Range (K)	Ref.	T_c (K)	S_{max} (J mol^{-1} K^{-1})
Sillimanite	Al_2SiO_5	1.60E+09	−1.24E+07	3.21E+03	0	1.84E+02	1.82E-02	0	0	298–3000	FactPS [49]	2200 26	4 26
Mullite	$Al_6Si_2O_{13}$	2.12E+09	−1.72E+07	0	−3.37E+03	6.35E+02	0	0	0	298–2163	FactPS [49]		
Gehlenite	$Ca_2Al_2SiO_7$	4.78E+08	−4.78E+06	0	−2.28E+03	3.73E+02	0	0	0	298–698	Berman	700 26	14 26
		4.78E+08	1.25E+07	0	−2.28E+03	1.51E+02	3.70E-01	−1.47E-04	0	698–1600	1985 [23]		
		4.78E+08	−4.78E+06	0	−2.28E+03	3.73E+02	0	0	0	1600–2500			
Akermannite	$Ca_2MgSi_2O_7$	−4.08E+07	0	0	−2.94E+03	3.87E+02	0	0	0	298–2000	Berman 1985 [23]		
Larnite	Ca_2SiO_4	3.08E+07	0	0	−2.03E+03	2.44E+02	0	0	0	298–2500	FToxid [49]	1710 26	10 26
	$Ca_2ZnSi_2O_7$	1.37E+09	−9.51E+06	0	−9.43E+02	3.29E+02	6.79E-03	0	0	298–2000	FToxid [49]		
Andradite	$Ca_3Fe_2Si_3O_{12}$	0	−6.79E+05	0	−7.40E+03	8.09E+02	−7.03E-02	0	0	298–3000	FToxid [49]	150 26	30 26
Merwinite	$Ca_3MgSi_2O_8$	−3.44E+08	0	0	−3.25E+03	4.54E+02	0	0	0	298–2500	Berman 1985 [23]		
Rankinite	$Ca_3Si_2O_7$	1.37E+09	−1.07E+07	0	−2.20E+03	3.93E+02	0	0	0	298–5000	FToxid [49]		
Wollastonite	$Ca_3Si_3O_9$	4.84E+08	−3.66E+06	0	−6.90E+02	1.49E+02	0	0	0	298–2000	Berman 1985 [23]		
	$Ca_3Ti_2O_7$	0	−5.72E+06	0	0	2.99E+02	1.59E-02	0	0	298–2023	FToxid [49]		
	$Ca_4Ti_3O_{10}$	0	−8.23E+06	0	0	4.24E+02	2.18E-02	−6.70E-08	0	298–2130	FToxid [49]		
		0	0	0	0	4.68E+02	0	0	0	2130–2500			
Anorthite	$CaAl_2Si_2O_8$	−3.17E+08	0	0	−3.73E+03	4.39E+02	0	0	0	298–1828	Berman	2300 26	11 26
		0	0	0	0	3.81E+02	0	0	0	1828–2500	1985 [23]		
Ca-tschermaks	$CaAl_2SiO_6$	9.61E+08	−5.34E+06	−2.71E+04	0	2.80E+02	2.69E-03	0	0	298–3000	FactPS [49]		
Ca-walstromite (pseudowolastonite)	$CaCa_2(Si_3O_9)$	9.41E+08	−5.86E+06	0	−4.17E+02	1.41E+02	0	0	0	298–1813	Berman 1985 [23]		
Hedenbergite	$CaFeSi_2O_6$	−4.78E+09	3.08E+07	−9.32E+04	0	3.09E+02	1.41E-02	0	0	298–3000	FToxid [49]	31 26	13 26

Table B.1(b)
C_p terms of the compounds used for training the Polyhedron model. The coefficients shown have been rounded for presentation, but the exact values were used in the regression analysis.

Name	Compound	T^{-3}	T^{-2}	T^{-1}	$T^{-0.5}$	T^0	T^1	T^2	T^3	T Range (K)	Ref.	T_c (K)	S_{max} (J mol^{-1} K^{-1})
Diopside	$CaMgSi_2O_6$	9.22E+08	−7.17E+06	0	−1.60E+03	3.05E+02	0	0	0	298–2000	Berman 1985 [23]		
Monticellite	$CaMgSiO_4$	−2.33E+07	−1.18E+06	0	−1.54E+03	2.26E+02	0	0	0	298–2000	Berman 1985 [23]		
Perovskite	$CaTiO_3$	0	−2.39E+05	0	0	2.91E+01	3.33E-01	−3.14E-04	0	298–475	FToxid [49]		
		0	−1.24E+06	0	0	1.12E+02	2.14E-02	−2.69E-06	0	475–2220			

(continued on next page)

Table B.1(b) (*continued*)

Name	Compound	T^{-3}	T^{-2}	T^{-1}	$T^{-0.5}$	T^{0}	T^{1}	T^{2}	T^{3}	T Range (K)	Ref.	T_c (K)	S_{max} (J mol^{-1} K^{-1})
Sphene	$CaTiSiO_5$	0	0	0	0	−3.38E+01	1.01E+00	−1.83E-03	1.33E-06	298–475	FToxid [49]		
		0	−5.91E+05	0	0	1.30E+02	1.24E-01	−5.41E-05	0	475–1200			
		0	0	0	0	2.01E+02	0	0	0	1200			
Ferrocordierite	$Fe_2Al_4Si_5O_{18}$	7.21E+09	−4.94E+07	0	−5.17E+02	7.85E+02	0	0	0	298–1500	FToxid [49]	1800 [26]	20 26
Ferrosillite	$Fe_2Si_2O_6$	2.93E+08	−2.10E+06	0	−1.19E+03	1.69E+02	0	0	0	298–2500	Berman 1985 [23]	40 [28, 87]	27 87
Fayalite	Fe_2SiO_4	−1.39E+08	0	0	−1.92E+03	2.49E+02	0	0	0	298–1478	Berman 1985 [23]	126 [87]	27 87
Ulvöspinel	Fe_2TiO_4	−5.45E+07	0	0	−1.82E+03	2.50E+02	0	0	0	298–2000	FactPS [49]	120 [87]	27 87
Ferropseudobrookite	$FeTi_2O_5$	4.56E+08	−4.50E+06	0	−1.03E+03	2.47E+02	0	0	0	298–1728	FactPS [49]	40 [28]	13.5 28
Ilmenite	$FeTiO_3$	3.48E+08	−3.32E+06	0	−4.42E+02	1.50E+02	0	0	0	298–1650	Berman 1985 [23]	40 [28]	13.5 28
Potassium disilicate	$K_2Si_2O_5$	2.29E+09	−1.48E+07	0	0	2.41E+02	0	0	0	298–1318	FToxid [49]		
	$K_2Si_4O_9$	3.27E+09	−2.19E+07	0	−4.81E+02	4.01E+02	0	0	0	298–373	FToxid		
		3.27E+09	−2.19E+07	0	−4.81E+02	4.01E+02	1.69E-02	−9.04E-05	1.21E-07	343–865	[49]		
		0	0	0	0	3.91E+02	1.62E-02	0	0	865–1038			
Potassium metasilicate	K_2SiO_3	0	−1.42E+06	0	0	1.19E+02	4.88E-02	0	0	298–1249	FToxid [49]		
Leucite	$KAlSi_2O_6$	9.59E+08	−7.86E+06	0	0	1.61E+02	2.92E-01	−4.30E-04	2.72E-07	298–850	FToxid [49]	938 [26]	18 26
		9.59E+08	−7.86E+06	0	0	−7.89E+04	2.75E+02	−3.20E-01	1.24E-04	850–918			
		0	−6.38E+06	0	0	2.41E+02	1.47E-03	0	0	918–2000			
Microcline	$KAlSi_3O_8$	1.21E+09	−8.55E+06	0	−2.42E+03	3.98E+02	0	0	0	298–1473	FToxid [49]		
Kalsilite	$KAlSiO_4$	2.14E+09	−1.31E+07	0	0	1.84E+02	9.85E-03	−4.65E-06	5.41E-10	298–2100	FToxid [49]		
Virgilite	$Li(AlSi_2O_6)$	0	0	0	−3.44E+03	3.63E+02	−3.68E-03	0	0	298–2000	FToxid [49]		
Petalite	$Li(AlSi_4O_{10})$	0	−6.74E+06	0	0	2.61E+02	2.24E-01	−8.93E-05	0	298–1250	FToxid[49]		

Table B.1(c)

C_p terms of the compounds used for training the Polyhedron model. The coefficients shown have been rounded for presentation, but the exact values were used in the regression analysis.

Name	Compound	T^{-3}	T^{-2}	T^{-1}	$T^{-0.5}$	T^{0}	T^{1}	T^{2}	T^{3}	T Range (K)	Ref.	T_c (K)	S_{max} (J mol^{-1} K^{-1})
Lithium disilicate	$Li_2Si_2O_5$	0	1.63E+06	−4.05E+04	0	2.58E+02	1.32E-02	0	0	298–1215	FToxid[49]		
Lithium metasilicate	Li_2SiO_3	0	−1.77E+06	0	−9.71E+02	1.71E+02	1.88E-02	0	0	298–1474	FToxid[49]		
Ramsdellite	$Li_2Ti_3O_7$	0	−3.72E+06	0	0	2.30E+02	1.25E-01	−6.19E-08	0	298–940	FToxid[49]		
		0	0	0	0	3.44E+02	0	0	0	940–1000			
	Li_2TiO_3	0	−1.95E+06	0	0	1.20E+02	4.68E-02	−1.21E-05	0	298–1820	FToxid[49]		
Spodumene	$LiAl(Si_2O_6)$	0	0	0	−3.44E+03	3.63E+02	−3.68E-03	0	0	298–2000	FToxid[49]		
Eucryptite	$LiAl(SiO_4)$	8.23E+08	−6.01E+06	0	−1.24E+03	2.19E+02	0	0	0	298–1500	FToxid[49]		
Cordierite	$Mg_2Al_4Si_5O_{18}$	−3.70E+08	−2.32E+06	0	−7.96E+03	9.54E+02	0	0	0	298–1750	Berman 1985[23]	1800[26]	20[26]
Enstatite (ortho-enstatite)	$Mg_2Si_2O_6$	0	−2.58E+06	0	0	1.08E+02	1.86E-02	0	0	298–2500	FToxid[49]		
Forsterite	Mg_2SiO_4	−1.16E+08	0	0	−2.00E+03	2.39E+02	0	0	0	298–3000	Berman 1985[23]		
Qandilite	Mg_2TiO_4	4.13E+07	−1.70E+06	0	−1.38E+03	2.26E+02	0	0	0	298–2029	FactPS[49]		
Pyrope	$Mg_3Al_2Si_3O_{12}$	0	−4.70E+06	0	−4.54E+03	6.41E+02	0	0	0	298–1700	Berman 1985[23]		
Sapphirine	$Mg_4Al_{10}Si_2O_{23}$	3.99E+09	−3.37E+07	0	−5.33E+03	1.17E+03	0	0	0	298–2000	FToxid[49]		
Karooite	$MgTi_2O_5$	5.82E+08	−5.66E+06	0	−7.55E+02	2.33E+02	0	0	0	298–1930	FactPS[49]		
Geikielite	$MgTiO_3$	4.02E+08	−4.00E+06	0	−4.16E+02	1.46E+02	0	0	0	298–1903	FactPS[49]		
Mn-cordierite	$Mn_2Al_4Si_5O_{18}$	5.61E+09	−3.82E+07	0	−1.66E+03	7.80E+02	1.62E-02	0	0	298–6000	FToxid[49]	1800[26]	20[26]
Tephroite	Mn_2SiO_4	0	4.60E+06	0	−6.64E+03	5.13E+02	−1.83E-01	5.21E-05	0	298–3000	FToxid[49]	40[28]	30[28]

(*continued on next page*)

Table B.1(c) (*continued*)

Name	Compound	T^{-3}	T^{-2}	T^{-1}	$T^{-0.5}$	T^{0}	T^{1}	T^{2}	T^{3}	T Range (K)	Ref.	T_c (K)	S_{max} (J mol^{-1} K^{-1})
Tetragonal	Mn_2TiO_4	0	−2.56E+06	0	0	1.68E+02	1.74E-02	0	0	298–2000	FactPS[49]	77[26]	30[26]
Rhodonite	$Mn_5Si_5O_{15}$	0	−3.04E+06	0	2.74E+02	9.90E+01	1.91E-02	0	0	298–2500	FToxid[49]	40[28]	75[28]
Pyroxmangite	$MnSiO_3$	0	−3.04E+06	0	2.74E+02	9.90E+01	1.91E-02	0	0	298–2500	FToxid[49]	40[28]	15[28]
Mn-pseudobrookite	$MnTi_2O_5$	4.56E+08	−4.50E+06	0	−1.03E+03	2.47E+02	0	0	0	298–2000	FactPS[49]	40[28]	15[28]
Pyrophanite	$MnTiO_3$	0	−2.19E+06	0	0	1.22E+02	9.29E-03	0	0	298–2000	FactPS[49]	40[28]	15[28]
Sodium disilicate	$Na_2Si_2O_5$	2.22E+09	−1.57E+07	0	0	2.51E+02	0	0	0	298–1148	FactPS[49]		

Table B.1(d)
C_p terms of the compounds used for training the Polyhedron model. The coefficients shown have been rounded for presentation, but the exact values were used in the regression analysis.

Name	Compound	T^{-3}	T^{-2}	T^{-1}	$T^{-0.5}$	T^{0}	T^{1}	T^{2}	T^{3}	T Range (K)	Ref.	T_c (K)	S_{max} (J mol^{-1} K^{-1})
	$Na_2Ti_3O_7$	1.14E+09	−1.05E+07	0	−3.28E+02	3.25E+02	−4.75E-03	8.48E-06	0	298–1403	FToxid[49]		
	$Na_2Ti_6O_{13}$	0	−6.24E+06	0	0	4.39E+02	1.23E-01	−2.56E-05	0	298–1573	FToxid[49]		
	Na_2TiO_3	0	−1.50E+06	0	0	1.18E+02	9.19E-02	−3.63E-05	0	298–1303	FToxid[49]		
	Na_2ZnO_2	0	−1.33E+06	0	0	1.04E+02	7.53E-02	−3.05E-05	0	298–1000	FactPS[49]		
Sodium orthosilicate	Na_4SiO_4	0	0	0	0	1.63E+02	7.42E-02	0	0	298–1358	FToxid[49]		
Sodium silicate	$Na_6Si_2O_7$	3.23E+09	−2.04E+07	0	−1.01E+03	4.61E+02	0	0	0	298–1397	FToxid[49]		
Monophyllosilicate	$Na_6Si_8O_{19}$	5.41E+09	−3.55E+07	0	−4.02E+03	9.88E+02	0	0	0	298–1082	FToxid[49]		
	$Na_8Ti_5O_{14}$	2.01E+09	−2.01E+07	0	0	6.54E+02	1.75E-01	−5.64E-05	0	298–1405	FToxid[49]		
		2.01E+09	−1.68E+07	0	0	8.08E+02	0	0	0	1405–1500			
		2.01E+09	−1.68E+07	0	0	8.08E+02	0	0	0	1500–2130			
		0	0	0	0	9.20E+02	0	0	0	2130–3000			
Albite	$NaAlSi_3O_8$	1.07E+09	−7.93E+06	0	−2.53E+03	3.98E+02	0	0	0	298–3000	FToxid[49]	950[26]	16[26]
Nepheline	$NaAlSiO_4$	2.02E+09	−1.04E+07	0	−8.79E+02	2.12E+02	0	0	0	298–3000	FToxid[49]	467[26]	10[26]
Aegirine (Acmite)	$NaFeSi_2O_6$	0	−3.61E+06	0	0	1.71E+02	1.49E-01	−5.96E-05	0	298–1263	FToxid[49]	50[26]	15[26]
	$Pb_2Al_2O_5$	3.18E+08	−3.86E+06	0	−9.60E+02	2.50E+02	2.45E-02	0	0	298–1159	FToxid[49]		
	$Pb_2Fe_2O_5$	4.35E+08	−5.58E+06	0	−1.32E+02	2.42E+02	2.45E-02	0	0	298–1250	FToxid[49]		
Melanotekite	$Pb_2Fe_2Si_2O_9$	1.42E+09	−1.27E+07	0	−6.12E+02	4.02E+02	2.45E-02	0	0	298–1250	FToxid[49]		
	Pb_2SiO_4	2.82E+09	−1.55E+07	0	0	2.06E+02	−3.66E-03	0	0	298–1016	FToxid[49]		
		0	0	0	0	1.89E+02	0	0	0	1016–1200			
	$Pb_2ZnSi_2O_7$	7.88E+08	−7.09E+06	0	−7.04E+02	3.04E+02	3.13E-02	0	0	298–1150	FToxid[49]		
	$Pb_3Ca_2Si_3O_{11}$	1.54E+09	−1.29E+07	0	−1.19E+03	5.01E+02	3.68E-02	0	0	298–2500	FToxid[49]		
	Pb_4SiO_6	0	−1.69E+06	0	0	2.23E+02	8.74E-02	0	0	298–999	FToxid[49]		
		0	0	0	0	3.08E+02	0	0	0	999–1200			
Calcium-lead barysilite	$Pb_8CaSi_6O_{21}$	2.69E+09	−2.24E+07	0	−2.10E+03	9.20E+02	9.80E-02	0	0	298–1124	FToxid[49]		
	$Pb_8ZnSi_6O_{21}$	2.48E+09	−2.13E+07	0	−2.06E+03	9.09E+02	1.05E-01	0	0	298–1064	FToxid[49]		

Table B.1(f)
C_p terms of the compounds used for training the Polyhedron model. The coefficients shown have been rounded for presentation, but the exact values were used in the regression analysis.

Name	Compound	T^{-3}	T^{-2}	T^{-1}	$T^{-0.5}$	T^{0}	T^{1}	T^{2}	T^{3}	T Range (K)	Ref.	T_c (K)	S_{max} (J mol^{-1} K^{-1})
	$PbAl_2O_4$	3.64E+08	−3.86E+06	0	−8.94E+02	2.03E+02	1.23E-02	0	0	298–1250	FToxid[49]		
	$PbCa_2Si_3O_9$	1.64E+09	−1.29E+07	0	−1.05E+03	4.05E+02	1.23E-02	0	0	298–1355	FToxid[49]		
	$PbFe_4O_7$	1.01E+09	−1.12E+07	0	−6.58E+01	3.41E+02	1.23E-02	0	0	298–1500	FToxid[49]		
	$PbSiO_3$	1.79E+09	−1.04E+07	0	0	1.40E+02	−1.54E-03	0	0	298–1033	FToxid[49]		
		0	0	0	0	1.30E+02	0	0	0	1033–1200			
	$PbZnSiO_4$	3.42E+08	−3.55E+06	0	−3.98E+02	1.76E+02	1.90E-02	0	0	298–1300	FToxid[49]		
	Zn_2SiO_4	1.56E+08	−2.53E+06	0	−6.86E+02	1.80E+02	1.36E-02	0	0	298–1800	FToxid[49]		
Zinc titanate	Zn_2TiO_4	0	−3.22E+06	0	0	1.67E+02	2.32E-02	0	0	298–2000	FactPS[49]		
Gahnite	$ZnAl_2O_4$	3.05E+08	−3.86E+06	0	−9.20E+02	2.03E+02	6.79E-03	0	0	298–2233	FactPS[49]		
Zinc ferrite	$ZnFe_2O_4$	0	0	−7.36E+03	−1.30E+03	2.38E+02	0	0	0	298–2500	FactPS[49]		

Data availability

Data will be made available on request.

References

[1] B. Ehrhart, E. Coker, N. Siegel, A. Weimer, Thermochemical cycle of a mixed metal oxide for augmentation of thermal energy storage in solid particles, Energy Proc. 49 (2014) 762–771.

[2] C.M. Vladut, D. Lincu, D. Berger, C. Matei, R.-A. Mitran, Molten bismuth–bismuth/zinc oxide composites for high-temperature thermal energy storage, INORGA 12 (5) (2024) 126.

[3] L.C. Walters, Nuclear fuel: design and fabrication, in: C.J. Cleveland (Ed.), Encyclopedia of Energy, Elsevier, New York, 2004, pp. 341–350.

[4] Y.S. Kim, H.T. Chae, S. Van den Berghe, A. Leenaers, V. Kuzminov, A.M. Yacout, Aluminum cladding oxide growth prediction for high flux research reactors, J. Nucl. Mater. 529 (2020) 151926.

[5] I. Şerban, A. Enesca, Metal oxides-based semiconductors for biosensors applications, Front. Chem. 8 (2020).

[6] M. Hariharan, R.D. Eithiraj, Unveiling the recently synthesis noncentrosymmetric layered $ASb_3X_2O_{12}$ (A = K, Rb, Cs, Tl; X = Se, Te) via first principles calculations, J. Phys. Chem. Solid. 196 (2025) 112388.

[7] F. Wang, D. Kozawa, Y. Miyauchi, K. Hiraoka, S. Mouri, Y. Ohno, et al., Considerably improved photovoltaic performance of carbon nanotube-based solar cells using metal oxide layers, Nat. Commun. 6 (1) (2015) 6305.

[8] S. Calnan, Applications of oxide coatings in photovoltaic devices, Coatings 4 (1) (2014) 162–202.

[9] A. Lucia, O. Gregory, Modeling thermophysical properties of glasses, Sci. Rep. 13 (1) (2023) 989.

[10] M.D. Mashitah, Y.S. Chan, J. Jason, Chapter 8 - antimicrobial properties of nanobiomaterials and the mechanism, in: A.M. Grumezescu (Ed.), Nanobiomaterials in Antimicrobial Therapy, William Andrew Publishing, 2016, pp. 261–312.

[11] Y. Kobayashi, T. Kondo, E. Ohtani, N. Hirao, N. Miyajima, T. Yagi, et al., Fe-Mg partitioning between (Mg, Fe)SiO_3 post-perovskite, perovskite, and magnesiowüstite in the Earth's lower mantle, Geophys. Res. Lett. 32 (19) (2005).

[12] L. Dubrovinsky, N. Dubrovinskaia, F. Langenhorst, D. Dobson, D. Rubie, C. Geßmann, et al., Iron–silica interaction at extreme conditions and the electrically conducting layer at the base of Earth's mantle, Nature 422 (6927) (2003) 58–61.

[13] I.H. Jung, S.A. Decterov, A.D. Pelton, Critical thermodynamic evaluation and optimization of the MgO-Al_2O_3, CaO-MgO-Al_2O_3, MgO-Al_2O_3-SiO_2 systems, JPEDAV 25 (2004) 17.

[14] I. Irikka, R. Zhang, L-g Xia, N. Hellsten, P.A. Taskinen, Thermodynamic assessment of ZnO-SiO_2 system, Trans. Nonferrous Metals Soc. China 28 (9) (2018) 8.

[15] O. Kubachewski, C. Alcock, P. Spencer, Materials Thermochemistry, sixth ed., Pergamon Press, UK, 1993.

[16] J. Robinson, T. Barry, Experimental Methods for the Measurement of Thermodynamic Data and Recommendation about the Future Capability at NPL, National Physical Laboratory, UK, 1997.

[17] J. Ding, N. Xu, M.T. Nguyen, Q. Qiao, Y. Shi, Y. He, et al., Machine learning for molecular thermodynamics, Chin. J. Chem. Eng. 31 (2021) 227–239.

[18] S. Kurth, M.A.L. Marques, E.K.U. Gross, in: F. Bassani, G.L. Liedl, P. Wyder (Eds.), Density Functional Theory, Encyclopedia of Condensed Matter Physics, Elsevier Ltd., 2005, pp. 395–402.

[19] C. Takoukam-Takoundjou, E. Bourasseau, V. Lachet, Study of thermodynamic propertis of $U_{1-y}Pu_yO_2$ MOX fuel using classical molecular Monte Carlo Simulations, J. Nucl. Mater. 534 (2020) 13.

[20] K. Kobayashi, M. Okumura, H. Nakamura, M. Itakura, M. Machida, M.W.D. Cooper, Machine learning molecular dynamics simulations toward exploration of high-temperature properties of nuclear fuel materials: case study of thorium dioxide, Sci. Rep. 12 (1) (2022) 9808.

[21] W. Latimer, Methods of estimating thermodynamic properties of compounds, J. Am. Chem. Soc. 73 (4) (1951) 1480–1482.

[22] H. Kopp, Investigations of the specific heat of solid bodies, Philos. Trans. Royal Soc. A. 155 (1865) 71–203.

[23] R.G. Berman Thb, Heat capacity of minerals in the system Na_2O-K_2O-CaO-MgO-FeO-Fe_2O_3- Al_2O_3-SiO_2- TiO_2- H_2O- CO_2, Contrib. Mineral. Petrol. 89 (1985) 15.

[24] H. Helgeson, J.M. Delany, H.W. Nesbitt, D.K. Bird, Summary and critique of rock forming minerals, Am. J. Sci. 278-A (1978) 43–66.

[25] J.A. Chermak, J.D. Rimstidt, Estimating the thermodynamic properties (ΔG_{fo} and ΔH_{fo}) of silicate minerals at 298 K from the sum of polyhedral contributions, Am. Mineral. 74 (1989) 8.

[26] T.J.B. Holland, Dependence of entropy on volume for silicate and oxide minerals: a review and a predictive model, Am. Mineral. 74 (1989) 5–13.

[27] V.J. Van-Hinsberg, S.P. Vriend, J.C. Schumacher, A new method to calculate end-member thermodynamic properties of minerals from their constituent polyhedra II: heat capacity, compressibility and thermal expansion, J. Metamorph. Geol. 23 (8) (2005) 681–693.

[28] V.J. Van Hinsberg, S.P. Vriend, J.C. Schumacher, A new method to calculate end-member thermodynamic properties of minerals from their constituent polyhedra I: enthalpy, entropy and molar volume, J. Metamorph. Geol. 23 (3) (2005) 165–179.

[29] T. Wu, E. Moosavi-Khoonsari, I.-H. Jung, Estimation of thermodynamic properties of oxide compounds from polyhedron method, Calphad 57 (2017) 107–117.

[30] E. Moosavi-Khoonsari, J.A. Arias-Hernandez, S.Y. Kwon, Review and perspective on polyhedron model for estimating thermodynamic properties of oxides, J. Am. Ceram. Soc. 107 (3) (2024) 1636–1647.

[31] J. Leitner, P. Chuchvalec, D. Sedmidubsky, A. Strejc, P. Abrman, Estimation of heat capacities of solid mixed oxides, Thermochim. Acta 395 (2002) 19.

[32] J. Leitner, P. Voňka, D. Sedmidubský, P. Svoboda, Application of Neumann–Kopp rule for the estimation of heat capacity of mixed oxides, Thermochim. Acta 497 (1–2) (2010) 7–13.

[33] H. Helgeson, Thermodynamic properties of hydrothermal systems at elevated temperatures and pressures, Am. J. Sci. 267 (1969) 75.

[34] P. Garofalo, A. Audetat, D. Gunther, C.A. Heinrich, J. Ridley, Estimation and Testing of Standard Molar Thermodynamic Properties of Tourmaline End-Members Using Data of Natural Samples American Mineralogist, vol. 85, 2000, p. 10.

[35] G.R. Robinson, J.L. Haas, Heat capacity, relative enthalpy, and calorimetric entropy of silicate minerals: an empirical method of prediction, Am. Mineral. 68 (1983) 12.

[36] R.M. Hanzen, A useful fiction: polyhedron modelling of mineral properties, Am. J. Sci. 228-A (1988) 242–269.

[37] A. La-Iglesia, J. Felix, Estimation of thermodynamic properties of mineral carbonates at high and low temperatures from the sum of polyhedral contributions, Geochem. Cosmochim. Acta 58 (19) (1994) 3983–3991.

[38] M.L. Boucher, D.E. Peacor, The crystal structure of alamosite, $PbSiO_3$, Z. Kristallogr. Cryst. Mater. 126 (1968) 111–198.

[39] L. Wang, P. Yuan, F. Wang, E. Liang, Q. Sun, Z. Guo, et al., First-principles study of tetragonal $PbTiO_3$: phonon and thermal expansion, Mater. Res. Bull. 49 (2014) 509–513.

[40] R. Powell, T.J.B. Holland, An enlarged and updated internally consistent thermodynamic dataset with uncertainties and correlations: the system K_2O-NaO-CaO-MgO-MnO-FeO-Fe_2O_3-Al_2O_3-TiO_2-SiO_2-C-H_2-O_2, J. Metamorph. Geol. 8 (1990) 89–124.

[41] R. Robie, Z. Bin, B. Hemingway, M. Barton, Heat capacity and thermodynamic properties of andradite garnet $Ca_3Fe_2Si_3O_{12}$ between 10 and 1000 K and revised values for $G_{298.15K}$ of hedenbergite and wollastionite, Geochem. Cosmochim. Acta 51 (1987) 6.

[42] H.T. Haselton, R.A. Robie, B.S. Hemingway, Heat capacities of synthetic hedenbergite, ferrobustamite and $CaFeSi_2O_6$ glass, Geochem. Cosmochim. Acta 51 (8) (1987) 2211–2217.

[43] L. Cemič, E. Dachs, Heat capacity of ferrosilite, $Fe_2Si_2O_6$, Phys. Chem. Miner. 33 (7) (2006) 457–464.

[44] F. Grønvold, A. Sveen, Heat capacity and thermodynamic properties of synthetic magnetite (Fe_3O_4) from 300 to 1050 K. Ferrimagnetic transition and zero-point entropy, J. Chem. Therm. 6 (9) (1974) 859–872.

[45] B. Smetana, M. Žaludová, M. Tkadlečková, J. Dobrovská, S. Zlá, K. Gryc, et al., Experimental verification of hematite ingot mould heat capacity and its direct utilisation in simulation of casting process, J. Therm. Anal. Calorim. 112 (1) (2013) 473–480.

[46] J.L. Verhaeghe, G.G. Robbrecht, W.M. Bruynooghe, On the specific heat of Mn Zn- and Ni Zn-Ferrite between 20°C and 350°C, Appli. Sci. Res. Section B 8 (1) (1960) 128–134.

[47] M.A. Carpenter, Thermochemistry of aluminium/silicon ordering in feldspar minerals, in: Physical Properties and Thermodynamic Behaviour of Minerals, 225, NATO ASI Series, Netherlands, 1988.

[48] H. U, D.R. W, Structural and other contributions to the third-law entropies of silicates, Geochem. Cosmochim. Acta 40 (1976) 24.

[49] C.W. Bale, E. Bélisle, P. Chartrand, S.A. Decterov, G. Eriksson, A.E. Gheribi, et al., FactSage thermochemical software and databases, 2010–2016, Calphad 54 (2016) 35–53.

[50] V. Watts, Introduction to Statistics an Excel-Based Approach, Canada Fanshawe College Pressbooks, 2022.

[51] Y. Ida, Anharmonic effect on heat capacity of solids up to the critical temperature of lattice instability, Phys. Rev. B 1 (6) (1970) 2488–2496.

[52] M.M. Murshed, T.M. Gesing, Anisotropic thermal expansion and anharmonic phonon behavior of mullite-type Bi2Ga4O9, Mater. Res. Bull. 48 (9) (2013) 3284–3291.

[53] T.R. Ravindran, A.K. Arora, T.A. Mary, Anharmonicity and negative thermal expansion in zirconium tungstate, Phys. Rev. B 67 (6) (2003) 064301.

[54] N.D. Chatterjee, R. Krüger, G. Haller, W. Olbricht, The Bayesian approach to an internally consistent thermodynamic database: theory, database, and generation of phase diagrams, Contrib. Mineral. Petrol. 133 (1) (1998) 149–168.

[55] C. Prewitt, E. Kirchner, A. Preisinger, Crystal structure of larsenite $PbZnSiO_4$, Z. Kristallogr. Cryst. Mater. 124 (1–6) (1967) 115–130.

[56] S.Z. Karazhanov, P. Ravindran, H. Fjellvåg, B.G. Svensson, Electronic structure and optical properties of $ZnSiO_3$ and Zn_2SiO_4, J. Appl. Phys. 106 (12) (2009).

[57] M. Fabián, P. Bottke, V. Girman, A. Düvel, K.L. Da Silva, M. Wilkening, et al., A simple and straightforward mechanochemical synthesis of the far-from-equilibrium zinc aluminate, $ZnAl_2O_4$, and its response to thermal treatment, RSC Adv. 5 (67) (2015) 54321–54328.

[58] S. da Silva Pedro, A. López, Sosman L. Pantoja, Zn_2TiO_4 photoluminescence enhanced by the addition of Cr^{3+}, SN Appl. Sci. 2 (1) (2019) 47.

[59] D.-G. Kim, B. Konar, I.-H. Jung, Thermodynamic optimization of the K_2O-Al_2O_3-SiO_2 system, Ceram. Int. 44 (14) (2018) 16712–16724.

[60] D.W. Fasshauer, B. Wunder, N.D. Chatterjee, Heat capacity of wadeite-type $K2Si_4O_9$ and the pressure-inducedstable decomposition of K-feldspar, Contrib. Mineral. Petrol. 131 (1998) 8.

[61] L. Pankratz, W. Weller, Thermodynamic Properties of Three Lithium-Aliminum Silicates, 7001, Bureau of mines report of investigation, 1967, p. 12.

[62] D.-G. Kim, M.-A.V. Ende, P. Hudon, I.-H. Jung, Coupled experimental study and thermodynamic optimization of the K_2O-SiO_2 system, J. Non-Cryst. Solids 471 (2017) 13.
[63] T. Tang, P. Chen, W. Luo, D. Luo, Y. Wang, Crystalline and electronic structures of lithium silicates: a density functional theory study, J. Nucl. Mater. 420 (1–3) (2012) 7.
[64] V. Kahlenberg, Structural chemistry of anhydrous sodium silicates – a review, Chimia 64 (2010) 6.
[65] I. Tsuyumoto, T. Moriguchi, Synthesis and lithium insertion properties of ramsdellite LixTiO2 anode materials, Mater. Res. Bull. 70 (2015) 6.
[66] D. Zherebetskyy, S. Lebernegg, G. Amthauer, M. Grodzicki, Magnetic structure of almandine, Phys. Chem. Miner. 39 (2012) 10.
[67] E. Dachs, C.A. Geiger, A. Benisek, Almandine: lattice and non-lattice heat capacity behavior and standard thermodynamic properties, Am. Mineral. 97 (2012) 11.
[68] R.A. Lange, I.S.E. Carmichael, J.F. Stebbins, Phase transitions in leucite ($KAlSi_2O_6$), orthorhombic $KAlSiO_4$, and their iron analogues ($KFeSi_2O_6$, $KFeSiO_4$), Am. Mineral. 71 (1986) 8.
[69] S.A.T. Redfern, Order-disorder phase transitions, Rev. Mineral. Geochem. 39 (1) (2000) 105–133.
[70] A.M.T. Bell, C.M.B. Henderson, ChemInform abstract: rietveld refinement of the structures of dry-synthesized $MFe_3Si_2O_6$ leucites (M: K, Rb, Cs) by synchrotron X-ray powder diffraction, ChemInform 26 (5) (1995).
[71] Y. Deng, C. Eames, J.-N. Chotard, F. Lalère, V. Seznec, S. Emge, et al., Structural and mechanistic insights into fast lithium-ion conduction in Li_4SiO_4–Li_3PO_4 solid electrolytes, J. Am. Chem. Soc. 137 (28) (2015) 9136–9145.
[72] R. Brandt, B. Schulz, Specific heat of some Li-compounds, J. Nucl. Mater. 152 (2) (1988) 178–181.
[73] B. Konar, P. Hudon, I.-H. Jung, Coupled experimental phase diagram study and thermodynamic modeling of the Li_2O-Na_2O-SiO_2 system, J. Eur. Ceram. Soc. 38 (4) (2018) 2074–2089.
[74] B. Konara, P. Hudon, I.-H. Jung, Coupled experimental phase diagram study and thermodynamic modeling of the Li2O-Na2O-SiO2 system, J. Eur. Ceram. Soc. 38 (2018) 15.
[75] K.K. Kelley, S.S. Todd, R.L. Orr, E.G. King, K.R. Bonnickson, Thermodynamic Properties of Sodium-Aluminum and Potassium-Aluminum Silicates, vol. 4955, Bureau of mines, 1953, p. 21.
[76] A. Benisek, E. Dachs, The accuracy of standard enthalpies and entropies for phases of petrological interest derived from density-functional calculations, Contrib. Mineral. Petrol. 173 (2018) 11.
[77] B. Konar, M.-A. Van Ende, I.-H. Jung, Critical evaluation and thermodynamic optimization of the Li-O, and Li_2O-SiO_2 systems, J. Eur. Ceram. Soc. 37 (5) (2017) 2189–2207.
[78] S.-Y. Tan, D.J. Payne, J.P. Hallett, G.H. Kelsall, Developments in electrochemical processes for recycling lead–acid batteries, Curr. Opin. Electrochem. 16 (2019) 83–89.
[79] I. Santoso, P. Taskinen (Eds.), Phase Equilibria of Na_2O-PbO-SiO_2 System between 900 and 1100 °C, GDMB Verlag, 2017. EMC 2017.
[80] M.I. Sayyed, BaO-doped B_2O_3-Na_2O-PbO-SiO_2 glasses: improved radiation shielding properties for protection applications, Silicon 16 (6) (2024) 2473–2479.
[81] K.A. Krakau, E.J. Mukhin, M.S. Geinrich, Equilibrium Diagram of the System Na_2O–PbO–SiO_2, 1949, pp. 15–38.
[82] X. Ling, E. Moosavi-Khoonsari, M. Barati (Eds.), Phase Equilibrium Study in the Sodium Metasilicate Primary Phase Field of PbO-Na_2O-SiO_2 System between 800 and 1000 °C, MOLTEN, Australia, 2024.
[83] R.K. Samudrala, S. Patel, V. Penugurthi, B. Manavathi, A.A. P, In vitro studies of B_2O_3–SiO_2–Na_2O–CaO–ZnO bioactive glass system, J. Non-Cryst. Solids 574 (2021) 121164.
[84] G. Malavasi, G. Lusvardi, A. Pedone, M.C. Menziani, M. Dappiaggi, A. Gualtieri, et al., Crystallization kinetics of bioactive glasses in the ZnO-Na_2O-CaO-SiO_2 system, J. Phys. Chem. A 111 (34) (2007) 8401–8408.
[85] R. Rodríguez-Ramírez, I. Romero-Ibarra, J. Vazquez-Arenas, Synthesis of sodium zincsilicate (Na_2ZnSiO_4) and heterogeneous catalysis towards biodiesel production via Box-Behnken design, Fuel 280 (2020) 9.
[86] A.E. Holland, E.R. Segnit, The ternary system Na_2O-ZnO-SiO_2, Aust. J. Chem. 19 (6) (1965) 8.
[87] R.S. Carmichael, Handbook of Physical Properties of Rocks, CRC Press, Boca Raton, 1982, p. 356.